

pubs.acs.org/journal/ascecg Research Article

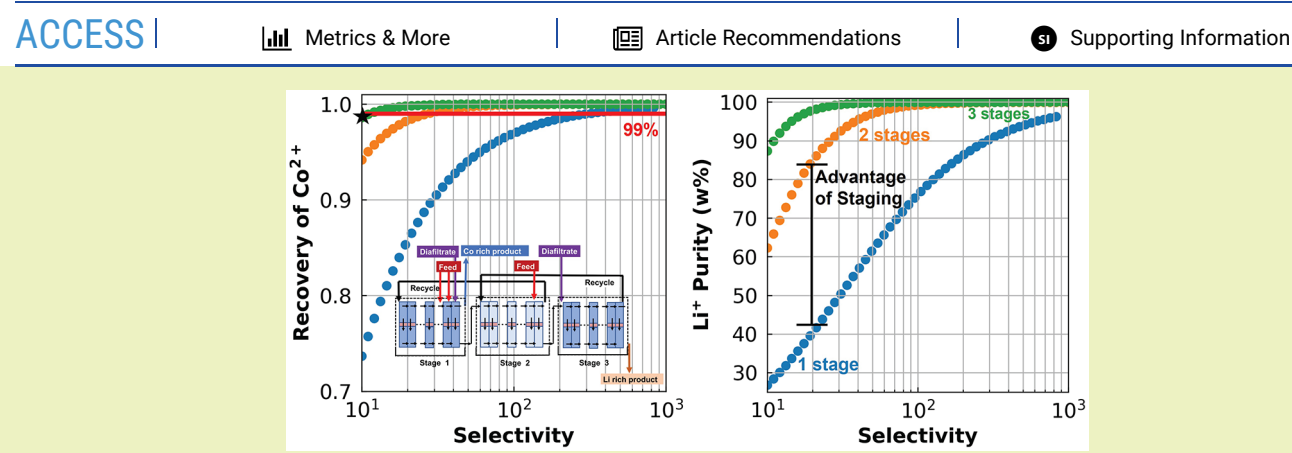
# Optimal Diafiltration Membrane Cascades Enable Green Recycling of Spent Lithium-Ion Batteries

Noah P. Wamble, Elvis A. Eugene, William A. Phillip, and Alexander W. Dowling\*



**Cite This:** ACS Sustainable Chem. Eng. 2022, 10, 12207–12225

Read Online



ABSTRACT: Novel processes are urgently needed to recycle critical materials (e.g., cobalt, lithium, nickel, and manganese) from spent lithium-ion batteries (LIBs). These separations are vital both to meet growing global demand and to mitigate a looming ewaste crisis. Currently, to recover cobalt and lithium from spent LIBs, high temperatures and organic solvents are used to separate Co<sup>2+</sup> and Li<sup>+</sup> in complex leaching and extraction processes. In contrast to using expensive designer ligands or harmful organic solvents, this work reveals that continuous membrane cascades are a promising aqueous-based alternative to recover these critical materials and facilitate their reuse. A superstructure optimization model that designs diafiltration cascades to maximize material recovery and purity as a function of membrane material performance and feed specifications is developed. This approach enables the comparison of candidate membrane materials by rapidly predicting the Pareto optimal trade-offs between the recovery and purity of lithium and cobalt for bespoke cascade designs. For example, the model predicts that, when deployed in an optimized two-stage cascade configuration, a nanofiltration membrane with a modest selectivity of 32 can be used to recover 95% Li<sup>+</sup> and 99% Co<sup>2+</sup> at 93 and 99.5 wt % purity, respectively. On the basis of analysis of over 1000 Pareto optimal designs, six design heuristics for executing binary separations using staged diafiltration cascades are proposed. Moreover, by evaluating membrane materials in the context of optimized diafiltration processes, this work quantifies the benefits of materials improvements and shows that the greatest research opportunities for membrane-based LIB recycling are at the device and systems scales. More broadly, the optimization models represent a robust framework for identifying the most effective way to deploy emerging materials in integrated process systems. This transformative capability is widely applicable to many of the separations needed to support sustainable global development.

KEYWORDS: Diafiltration, Fractionation, Multiscale modeling, Superstructure optimization, Design heuristics

#### INTRODUCTION

The growing demand for lithium, accelerated by plans for mass automobile electrification, is expected to outpace the limited global supply within the next decade. For example, General Motors announced plans to only sell zero-emission electric vehicles in the light-duty segment by 2035. Similarly, Tesla's stock price increased over 740% in 2020 suggesting broad support and anticipation of an electric vehicle (EV) future. Bohlsen predicts that the global demand for lithium carbonate equivalents may reach 2830 kilotons (kt) per year, but global production may only grow to 1430 kt per year, resulting in a significant deficit of 1400 kt per year. Sonoc et al. conclude that 100% of LIBs need to be recycled with a minimum 90% recovery

of lithium to have enough lithium carbonate equivalent for all of the 21st century. Yet, only 3% of lithium-ion batteries (LIBs) are currently recycled with the focus being on the more valuable components such as cobalt. In addition to their economic value, LIB components such as lead and cobalt are toxic and can harm human health and the environment if not properly disposed or

Received: May 14, 2022 Revised: August 10, 2022 Published: September 2, 2022





recycled.<sup>6</sup> New processes for recovering the components of LIBs are essential for creating a circular economy that both averts the anticipated supply crises and protects the environment.<sup>5</sup> Here, there is an opportunity for new separation technologies to recover LIB components as distinct high-purity products to facilitate reuse and offset the net cost of recycling.

Currently, there are no sustainable and economically feasible processes to recycle LIBs at the commercial scale. 7,8 Conventional recycling processes rely on hydrometallurgical techniques to leach or dissolve cathode elements in strong acids followed by a series of solvent extraction and chemical precipitation steps to separate and recover valuable metals. The recovery of highpurity metal-rich solutions in the recycling process necessitates the use of large quantities of solvents that tend to be toxic and harmful to the environment. 10,11 Sequential precipitation and coprecipitation are used to separate metal ions, but these methods are highly sensitive to the composition of the spent cathodes. 12 This sensitivity requires precise control of process conditions (e.g., pH, temperature), which is complicated by the heterogeneous composition of LIBs on the market. To mitigate these challenges, alternative fractionation techniques are being studied. Mild organic solvents which pose fewer threats to the environment are being employed in simultaneous leaching and precipitation steps for the selective recovery of metal ions from spent LIBs.<sup>13</sup> However, chelation in organic solvents makes metal ion precipitation more difficult to achieve when compared with precipitation from mineral acids. Selective dissolution techniques enable the recovery of high-purity metals but require several high-temperature operations. <sup>14</sup> Electrochemical techniques are also popular for the separation of metal ions but are energy-intensive.

Membrane separations are a promising, but mostly unexplored, technology to enable LIB recycling. Compared to solvent extraction, membrane separations avoid energyintensive regeneration and often occur in aqueous environments.<sup>16</sup> More efficient fractionation with membranes can replace complex coprecipitation steps to recover lithium, cobalt, and other valuable LIB components as high-purity products, ultimately enabling simpler, less-energy intensive, and more economic LIB recycling processes. Even though the hydrated radii of Li<sup>+</sup> and Co<sup>2+</sup> differ by only 0.41 Å, <sup>17</sup> nanofiltration membranes capable of separating these cations based on the differences in charge density with moderate selectivity exist. 18-22 As the need for more efficient Li<sup>+</sup> extraction and recovery processes expands, there is significant interest in emerging membrane materials that are tailored to exhibit uniquely high and selective rates of lithium transport. These membranes seek to utilize advanced materials that provide precise control over the membrane pore size, structure, and chemistry such that the thermodynamic partitioning and transport rate of Li<sup>+</sup> relative to other ions can be tailored. For example, MOF-based membranes with sub-nanometer pores allow Li<sup>+</sup> ions to partially dehydrate and partition into their crystalline structure, which results in Li<sup>+</sup> permeating selectively relative to other cations.<sup>18</sup>

While the recent advances in materials for the separation of lithium are indeed exciting, the synthesis of advanced materials in the past three decades has failed to produce a corresponding revolution in sustainable separation applications.<sup>23</sup> This is because seldom do materials innovations alone precipitate transformative technologies; more often, innovations require holistic molecular-to-systems engineering.<sup>24,25</sup> In this regard, diafiltration is a promising membrane-based technology to

execute the fractionation of lithium and cobalt. In conventional filtration processes, as the solution permeates through the membrane the concentration of the retained species increases. If this concentration approaches the solubility limit, salt can precipitate on the membrane surface hindering permeation and preventing the extraction of high-purity products. This solubility limit also prevents the direct staging of membrane units. In diafiltration processes, a dilute solution, known as the diafiltrate, is added to the feed side of a membrane to offset concentration effects. This management of the concentration profiles allows for the staging of membrane modules to form diafiltration cascades that enable the recovery of retentate and permeate streams enriched in the less permeable and more permeable solute, respectively. Yet, since development starting in the 1960s, <sup>26-34</sup> diafiltration has only expanded to niche applications that require high-purity, high-value products such as protein purification<sup>35</sup> and in the food and beverage industry.31 In this study, we propose a novel diafiltration membrane process to recover lithium and cobalt in high-purity from a leach liquor without extreme operating conditions or harsh solvents.

Thus, this paper uses process design via computational optimization to explore how to best deploy ion-selective nanofiltration membranes in diafiltration cascades for the recovery of valuable products, e.g., lithium and cobalt. These optimization tools facilitate fair and direct comparison of existing and emerging materials in the context of integrated separation systems using performance metrics such as purity and recovery. Computational optimization is necessary because designing large-scale diafiltration cascades involves hundreds of degrees of freedom arising from many staging and configuration options; enumerating all of these alternatives with classical process simulation tools is often not feasible.<sup>36</sup> Superstructure optimization, in contrast, is a well-established process systems engineering tool to rigorously search through design alternatives to minimize one or more quantitative objectives.<sup>37–39</sup> In superstructure optimization, a superstructure consisting of the component unit operations and modules that may constitute a process is proposed, and a mathematical model that encodes all reasonable system configurations is developed. Computational optimization is then used to search over the superstructure (and accompanying model) to determine the best system connectivity. Depending upon the scale examined, the optimal solution may identify recycle strategies in the flowsheet or technology alternatives in conceptual process design. In the context of membrane separations, superstructure optimization has helped reveal novel process configurations and systematically quantify design trade-offs for diverse applications including water treatment and desalination,  $^{40-47}$  hydrocarbon and biogas processing,  $^{48-52}$  and  $\mathrm{CO}_2$  capture.  $^{53-56}$ 

In this work, we use superstructure optimization to determine the best feed input locations, recycling strategies, split fractions, number of stages, and membrane area as a function of membrane transport characteristics at the materials scale and purity and recovery targets at the systems scale. For simplicity, it is assumed that the performance of the membrane materials can be described by constant transport coefficients. Future efforts can incorporate transport coefficients that depend on solution properties such as solute concentration, ionic strength, or pH into the mathematical framework. Even for constant transport coefficients, multiobjective optimization methods are needed to quantify the Pareto optimal trade-offs between purity and recovery of Li<sup>+</sup> and Co<sup>2+</sup>. This means for a given membrane material performance and feed specifications, there is not a

single best diafiltration cascade design but a set of optimal designs that offers different compromises across competing objectives.

The main contribution of this paper is the synthesis and analysis of staged diafiltration processes for lithium and cobalt fractionation. Inspired by the recent call from the U.S. National Academies to accelerate separation science with multiscale modeling, 57 this work is the first application of superstructure optimization to systematically design diafiltration systems. Through this new modeling approach, we rapidly explore how system design and performance (e.g., lithium and cobalt recovery trade-offs) depend on the membrane material properties (e.g., selectivity), the number of stages, and other design decisions. Thus, the proposed modeling framework facilitates the comparison of membrane materials in the context of optimized systems in contrast to the current practice of comparisons using a one-size-fits-all system which may not fully leverage the advances of each candidate membrane. Ultimately, we show diafiltration is a promising separation technology to fractionate lithium and cobalt using existing nanofiltration membranes, which emphasizes the importance of device and systems scale research for LIB recycling. Moreover, from a library of 1000 Pareto optimal cascades configurations, we identify and physically justify six new heuristics for diafiltration system design which are generally applicable to many environmentally important separations of ions beyond LIB recycling.

#### METHODS

Problem Statement. We postulate a continuous, multistage diafiltration cascade to fractionate Li<sup>+</sup> and Co<sup>2+</sup> in LIB recycling processes. The membranes within the cascade allow for the preferential permeation of lithium over cobalt under the action of pressure-driven flow. 19,58,59 As such, the solution that permeates through the membrane will be enriched in Li<sup>+</sup> relative to Co<sup>2+</sup>; the opposite will be true for the retained solution. A fresh diafiltrate stream, which can enter into the retentate side of any stage, is used to balance the flows of solution within the system, ensuring that the process can operate continuously at the pseudo-steady-state. Additionally, the diafiltrate reduces the concentration of the dissolved salts to prevent their precipitation, which would lead to membrane scaling and reduced performance. The retentate from each stage is either recycled back to the previous stage or removed as a Co-rich product. The solution that permeates through the membrane continues along the cascade as the feed stream to the next stage where this process is then repeated. The permeate stream from the last stage is collected as the lithium-enriched product. The performance of the membranes deployed in the cascade is described quantitatively by the solvent flux across the membrane,  $J_w$ , as well as the sieving coefficients for Li<sup>+</sup> and Co<sup>2+</sup>, S<sub>Li</sub><sup>+</sup> and S<sub>Co</sub><sup>2+</sup>, respectively. The selectivity of the membranes is given by  $\alpha = S_{\text{Li}^+}/S_{\text{Co}^{2+}}$ .

Given these membrane performance parameters and several system specifications—(a) total flow rate of the fresh feed (e.g., from a prior step in an integrated LIB recycling process), (b) concentration of Li<sup>+</sup> and Co<sup>2+</sup> in the fresh feed, (c) total flow rate of the fresh diafiltrate, (d) concentration of Li<sup>+</sup> and Co<sup>2+</sup> in the fresh diafiltrate, and (e) number of stages in the cascade—we seek to optimize the connectivity, flow rates, and concentration profiles within the multistage cascade to maximize both the recovery of Co<sup>2+</sup> in the retentate and the Li<sup>+</sup> in the permeate product streams. This is an inherently multiobjective optimization problem, and we seek to quantify the trade-offs between the recovery of Co<sup>2+</sup> and Li<sup>+</sup> by computing a set of Pareto optimal solutions. In the context of this problem, a diafiltration cascade design is Pareto optimal if it is not possible to improve one objective (e.g., maximize Co<sup>2+</sup> recovery) without sacrificing the other objectives (e.g., maximize Li+ recovery). 60,61 Thus, the proposed approach computes sets of Pareto optimal designs—not a single design—for a given set of membrane performance parameters and system specifications. This is a distinction

from some prior applications of superstructure optimization to membrane systems that report a single distinct solution for a singleobjective optimization problem (e.g., minimize cost with all performance metrics converted to monetary units).

By formulating module and cascade design as a multiobjective mathematical optimization problem, we systematically study multiscale decisions across the materials- and systems-scales for the development of continuous diafiltration cascades in sustainable LIB recycling. Specifically we investigate the following:

- What is the multiobjective (i.e., Pareto optimal) trade-off between Li<sup>+</sup> and Co<sup>2+</sup> recovery for a given set of membrane and system specifications?
- How do the Pareto optimal trade-off, required membrane area, and system connectivity change as the number of stages in the cascade increases?
- What general design heuristics for diafiltration cascades can be ascertained from a large library of optimized designs?
- How does molecular engineering of the membrane materials to increase selectivity, e.g., by manipulating S<sub>Li</sub>+ and S<sub>Co</sub><sup>2+</sup>, impact the performance of multistage cascades?

The remainder of this section describes our superstructure optimization approach, mathematical models, and solution strategy for this problem. The next section, Results and Discussion, utilizes the solution approach to compute Pareto efficient designs as a function of system and membrane property specifications and establish six design heuristics for continuous diafiltration cascades.

Optimization Superstructure. A superstructure system containing an arbitrary N-stage diafiltration cascade, as shown in Figure 1, is developed based on the prior problem statement. The superstructure system utilizes material balances and governing transport equations to encapsulate the abundance of decisions that membrane scientists and engineers face when designing a cascade. In the superstructure developed here, each stage is discretized into M = 10 finite elements. Often, membrane separations are deployed in skids that contain multiple membrane modules in series. Thus, to realize cascades encoded in the superstructure, each stage would correspond to a skid and each finite element representing a membrane module. Within each stage (skid), all finite elements (membrane modules) are constrained to be the same size (e.g., membrane area). For all finite elements l except the last in each stage, (e.g.,  $\forall l \in \{1, ..., M-1\}$ ), the retentate moves to the next element l + 1 (green arrows in Figure 1) and across the membrane (brown arrows) to the permeate. Likewise, all of the permeate in element l moves to the permeate in element l + 1 (pink arrows). System inputs of fresh feed (red arrows) and diafiltrate (purple arrows) can be injected at any element in the cascade. Staging is realized by directing the permeate stream (brown arrows) from the final element of one stage to enter as the feed of the next stage. Similarly, the Co<sup>2+</sup>-enriched retentate stream is withdrawn from the final element of each stage and can be recycled back to the prior stage (black arrows) or collected as a product stream (blue arrow) or both. When recycled, the stream (black arrows) can enter any element or elements on the feed side of the preceding stage. The permeate stream from stage N at the end of the cascade is always recovered as the Li+-enriched product (orange arrow). Through this modeling approach, streams can be distributed among a network of smaller flows on the stage and element levels, thereby allowing the superstructure framework to optimize over all possible process configurations and connectivities. Furthermore, by bounding solutions with physical constraints such as solubility limits, the model encodes into it all of the physically feasible solutions. This approach exploits many more degrees of freedom, or rather design decisions, to search for novel system configurations making it more rigorous than conducting a sensitivity analysis over a single process configuration. For example, the superstructure optimization model facilitates the comparison of isotropic cascades, which constrain each stage (skid) to the same area (to reduce complexity), and anisotropic cascades, which remove this constraint for additional degrees of freedom. In addition to identifying and quantifying the intuitive tradeoffs that engineers must manage, this model and its solutions reveal

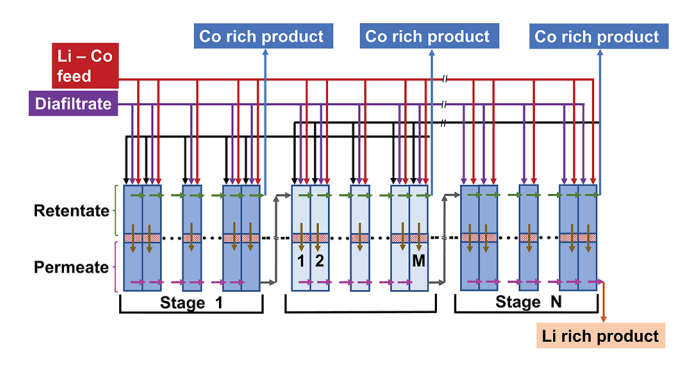


Figure 1. Superstructure model for a continuous diafiltration membrane cascade encodes all possible connectivities for an N-stage system. Each stage is divided into M elements. The red and purple arrows indicate the fresh feed and diafiltrate inflow streams, respectively. A flow rate of 100 m<sup>3</sup> h<sup>-1</sup> was assumed for the fresh feed. Unless stated otherwise, a diafiltrate flow of 30  $\mathrm{m}^3~\mathrm{h}^{-1}$  into the system was assumed. Moreover, it was assumed that the fresh feed contained 17 kg m<sup>-3</sup> and 1.7 kg m<sup>-3</sup> of cobalt and lithium, respectively.<sup>62</sup> The fresh diafitrate was assumed to contain 0.2 kg m<sup>-3</sup> cobalt and 0.1 kg m<sup>-3</sup> lithium to simulate impurities from reprocessed streams. Both of these streams may be subdivided and enter any finite element (labeled 1 to *M*) of any stage (labeled 1 to *N*). Within each stage, the retentate, shown by the green arrows, is enriched in the less permeable solute Co<sup>2+</sup> and may be withdrawn from the final element of the feed side and split into a product stream, shown by the blue arrows, or recycled as diafiltrate to the previous stage, as shown by the black arrows. The solution within each stage is filtered across the membrane, shown by the brown arrows, and produces a permeate stream enriched in the more permeable solute Li+ as indicated by the pink arrows. The dark gray arrows indicate the interstage connectivity which is realized by allowing the permeate leaving the last element of each stage to enter the first element of the following stage as the feed stream. The permeate product, lithium, is withdrawn from the final element of the last stage, as shown by the tan arrow. The optimization problem solution assigns a value of zero (0) to the vast majority of flow streams. Thus, the optimum cascade configuration is defined by the nonzero flow streams.

unexpected opportunities and trade-offs due to the nature of how this problem is constructed.

**Mathematical Model.** Using the diafiltration cascade superstructure, we formulate and solve mathematical optimization problems using Pyomo, an open-source Python-based algebraic modeling language, Ipopt, an open-source nonlinear programming algorithm, and the HSL sparse linear algebra routines. 63–65 We now describe the mathematical model in detail, which is adapted from our prior conference paper. 66

Assumptions. As demonstrated by prior experiments, a key advantage of staged designs is that they facilitate the continuous operation of diafiltration processes. 35,67,68 Therefore, within the superstructure (Figure 1), we assume the system operates continuously at steady state. Additionally, we assume the membrane performance is adequately characterized by a constant water flux  $J_w$ , which is supported by prior experimental validation. <sup>33,34</sup> Likewise, we assume the sieving coefficients  $S_{\text{Li}^+}$  and  $S_{\text{Co}^{2+}}$  are constant, which holds for some nanofiltration membranes<sup>33</sup> but breaks down for others.<sup>19,69,70</sup> It is easy mathematically to accommodate concentration-dependent sieving coefficients in the optimization framework, although experimentally developing and validating such correlations is left for future work. The goal of this study is to understand module and cascade design trade-offs as a function of these membrane performance metrics. Therefore, the relationships between these metrics and the solute and hydraulic permeability coefficients are not considered. These relationships, along with empirical correlations (e.g., those encoded within the permeability-selectivity trade-off) that constrain the values of the permeability coefficients or capture their variations in complex multicomponent solutions, can be incorporated in future iterations of the superstructure optimization framework. Similarly, concentration polarization is not considered explicitly because the system is assumed to operate at constant  $J_{\rm w}.^{71-73}$  This phenomenon would enter into the model by simply changing the assumed value of the sieving coefficients and would yield results similar to the sieving coefficient sensitivity analysis presented in this study.  $^{34,73}$  Lastly, this work focuses on the simplest case of binary fractionation of Li $^{+}$  and Co $^{2+}$  in an idealized feed. Extending the optimization framework to consider many components requires specifying additional sieving coefficients and possibly augmenting the superstructure to consider removal of other products, purge streams, or additional recycle streams.

Sets and Subscripts. The following sets are used to compactly define the mathematical model:

$$I = \{\text{Li, Co}\} \text{ (solutes)}$$

$$\mathcal{J} = \{ff, fd, rd, sf, f, r, fl, p, pr, re\} \text{ (all flow streams)}$$

$$\mathcal{J}_1 = \{ff, fd, rd, sf, f, r, fl, p\} \subset \mathcal{J} \text{ (inlet streams)}$$

$$\mathcal{J}_2 = \{pr, re\} \subset \mathcal{J} \text{ (retentate side stage outlets)}$$

$$\mathcal{J}_3 = \{ff, fd, rd, sf\} \subset \mathcal{J}_1 \text{ (feed side inlets)}$$

$$\mathcal{J}_4 = \{r, fl\} \subset \mathcal{J}_1 \text{ (element outlets)}$$

$$\mathcal{J}_5 = \{ff, fd\} \subset \mathcal{J}_1 \text{ (system inlets)}$$

$$\mathcal{K} = \{1, 2, ... N\} \text{ (stages)}$$

$$\mathcal{L} = \{1, 2, ... M\} \text{ (elements)}$$

Set I contains all the solutes considered in the system. Set J contains all the flow streams: ff is the fresh feed, fd is the fresh diafiltrate, rd is the recycled diafiltrate, sf is the stage feed, f is the element feed, r is the retentate, fl is the flux across the membrane, p is the permeate, pr is the retentate product, and re is the recycled retentate. Subsets  $J_1, ..., J_s$  are described above and used to define specific equations. Sets K and L denote the stages and elements, respectively.

Parameters. Table 1 lists the model parameters, which are fixed input data for the optimization problem. In a sensitivity analysis, one or more parameters are systematically varied.

The four key parameters describe the membrane material performance and module specifications. We assume the flux solvent flux across the membrane,  $J_{\rm w}=0.1~{{\rm m}^3~^{74}\over{{\rm m}^2~{\rm h}}}$  remains constant. Likewise, the stage width w is fixed as 1.5 m. Unless otherwise noted, the sieving coefficients  $S_{\rm Li^+}$  and  $S_{\rm Co}^{2+}$  were fixed at 1.3 and 0.5 for low selectivity

Table 1. Parameters in the Superstructure Optimization Problem

symbol	units	description
$n_{ m solutes}$	unitless	number of ion species
$Q_{ff}$	$\mathrm{m}^3~\mathrm{h}^{-1}$	amount of total fresh feed entering cascade
$C_{Co^{2+},ff}$	${\rm kg}~{\rm m}^{-3}$	concentration of Co <sup>2+</sup> in the fresh feed
$C_{\mathrm{Li}^+,ff}$	$kg m^{-3}$	concentration of Li <sup>+</sup> in the fresh feed
$Q_{fd}$	$m^3 h^{-1}$	amount of total fresh diafiltrate entering cascade
$C_{\operatorname{Co}^{2+},fd}$	${\rm kg}~{\rm m}^{-3}$	concentration of Co2+ in the fresh diafiltrate
$C_{\mathrm{Li}^+,fd}$	${\rm kg}~{\rm m}^{-3}$	concentration of Li <sup>+</sup> in the fresh diafiltrate
$J_{\rm w}$	$m^3 m^{-2} s^{-1}$	solvent flux across membrane
$S_{Li}^{+}$	unitless	lithium sieving coefficient
$S_{Co}^{^{2+}}$	unitless	cobalt sieving coefficient
α	unitless	selectivity, $\alpha = S_{\text{Li}^{+}}/S_{\text{Co}^{2}}+$
w	m	stage width
N	unitless	number of stages
M	unitless	number of elements
$R^*$	unitless	minimum lithium recovery

membranes and 0.75 and 0.05 for nanofiltration membranes for lithium and cobalt, respectively, based on typical values from the literature. The Specifying the sieving coefficients fixes the selectivity  $\alpha = S_{\rm Li} + /S_{\rm Co}^{2+}$ .

Unless otherwise noted, the following data are used to specify the case studies. We assume the fresh feed has a flow rate of  $Q_{ff} = 100 \text{ m}^3/\text{h}$  and contains  $C_{\text{Li},ff} = 1.7 \text{ kg/m}^3$ , and  $C_{\text{Co},ff} = 17 \text{ kg/m}^3$ . These concentrations are typical for leaching spent LIBs with hydrochloric acid. For the fresh diafiltrate, we assume a flow rate of  $Q_{fd} = 30 \text{ m}^3/\text{h}$  with concentrations  $C_{\text{Li},fd} = 0.1 \text{ kg/m}^3$  and  $C_{\text{Co},fd} = 0.2 \text{ kg/m}^3$ . The diafiltrate has some contamination in it to represent the diafiltrate being recycled in this process. The number of stages N and minimum lithium recovery  $R^*$  are systematically varied in the case studies. Each stage is discretized into M = 10 finite elements.

Optimization Variables. Table 2 describes the optimization decision variables, which are manipulated to minimize (or maximize)

Table 2. Optimization Variables in the Superstructure Model

symbol	units	description
$c_{i,j,k,l}$	${\rm kg}~{\rm m}^{-3}$	concentration of solute $i$ in stream $j$ in stage $k$ and finite element $l$
$q_{j,k,l}$	$m^3\;h^{-1}$	flow rate for stream $j$ in stage $k$ and finite element $l$
$l_k$	m	length of stage k
$A_{\mathrm{m}}$	m	total amount of membrane area
$\theta_k$	unitless	stage cut for stage k
I	kg m <sup>-3</sup>	sum of the concentration of impurities leaving each product stream

the objective function. For each stream in the superstructure, the flow rate q and concentration  $c_i$  are modeled with continuous variables. At an optimal solution, many of these flow rates within the system are set to zero per the superstructure shown in Figure 1, which indicate the corresponding connectivity is not realized. Regarding the membrane module design, the stage lengths  $l_k$  are used to compute the total membrane area  $A_{\rm m}$ . Likewise, the stage cuts  $\theta_k$  are continuous optimization variables.

Many of the optimization variables are also bounded, as described in Table 3, to both ensure physically meaningful solutions and improve

Table 3. Bounds for Optimization Variables

symbol	values	description
$\overline{q}$	10,000 m <sup>3</sup> h <sup>-1</sup>	maximum flow rate value within the system
$\frac{\overline{q}}{q_{\rm r}}$	$500 \text{ m}^3 \text{ h}^{-1}$	maximum recycle flow rate
$\underline{R}_{Co}$	0.005 unitless	minimum Co2+ recovery value for the system
$\overline{R_{\mathrm{Co}}}$	1 unitless	maximum Co2+ recovery value for system
$rac{L}{L}$	0.1 m	minimum stage length
$\overline{L}$	10,000 m	maximum stage length
$rac{ heta}{\overline{ heta}}$	0.01 unitless	minimum stage cut
$\overline{ heta}$	0.99 unitless	maximum stage cut
$\epsilon_{\mathrm{Li}^{^{+}}}$	$20 \text{ kg m}^{-3}$	concentration upper bound for Li <sup>+78</sup>
$\overline{c}_{Co}^{2+}$	$200 \text{ kg m}^{-3}$	concentration upper bound for Co <sup>2+78</sup>
$\underline{A}_{\mathrm{m}}$	0 m	lower bound for total membrane area
$\frac{\underline{A}_{\mathrm{m}}}{\overline{A}_{m}}$	30,000 m	upper bound for total membrane area

the numerical performance of the model. We use underbars and overbars to indicate lower and upper bounds, respectively. For several variables, e.g., stage length, the upper bound is so large it is not active at the solution. The concentration bounds for Li<sup>+</sup> and Co<sup>2+</sup> are based on their solubility limits in water. <sup>78</sup> The Li<sup>+</sup> upper bound was lowered from the solubility limit to improve numerical performance but was still higher than 10 times the incoming feed Li<sup>+</sup> concentration. With the exception of Co<sup>2+</sup> concentration in the retentate product at high Li<sup>+</sup> recovery, the concentrations in the optimal solutions are far from these bounds.

Mass Balance Constraints. Equation 1 requires the total fresh feed and fresh diafiltrate summed across all stages and elements equal to the system specifications  $(Q_j)$ . Similarly, eq 2 bounds the flow rates in each

element. Finally, eq 3 enforces the feed concentrations match the specifications for the incoming streams.

$$\sum_{k \in \mathcal{K}} \sum_{l \in \mathcal{L}} q_{j,k,l} = Q_j \quad \forall j \in \mathcal{J}_{S}$$

$$\tag{1}$$

$$q_{j,k,l} \le Q_j \quad \forall j \in \mathcal{J}_5, \ k \in \mathcal{K}, \ l \in \mathcal{L}$$
 (2)

$$c_{i,j,k,l} = C_{i,j} \quad \forall \ i \in I, \ j \in \mathcal{J}_5, \ k \in \mathcal{K}, \ l \in \mathcal{L}$$
 (3)

Equations 4 and 5 model the overall and component mass balances, respectively, for the inlet mixer in each element.

$$\sum_{j \in \mathcal{J}_3} q_{j,k,l} = q_{f,k,l} \quad k \in \mathcal{K}, \ l \in \mathcal{L}$$
 (4)

$$\sum_{j \in \mathcal{J}_3} (q_{j,k,l} \times c_{i,j,k,l}) = q_{f,k,l} \times c_{i,f,k,l} \ \forall \ i \in I, \ k \in \mathcal{K}, \ l \in \mathcal{L}$$
 (5)

Equations 6 and 7 model the feed side finite element of a membrane stage using overall and component mass balances.

$$\sum_{j} q_{j,k,l} = q_{f,k,l} \ \forall j \in \mathcal{J}_4, \ k \in \mathcal{K}, \ l \in \mathcal{L}$$

$$\tag{6}$$

$$\sum_{j} q_{j,k,l} \times c_{i,j,k,l} = q_{f,k,l} \times c_{i,f,k,l} \ \forall \ i \in I, \ j \in \mathcal{J}_4, \ k \in \mathcal{K}, \ l$$

$$\in \mathcal{I}. \tag{7}$$

A splitter is used at the end of every stage to divide the retentate into product and recycle streams, governed by eqs 8 and 9. These streams then are constrained to have the same concentration values as they all come from the same source.

$$\sum_{j} q_{j,k,M} = q_{r,k,M} \ \forall \ j \in \mathcal{J}_2$$
(8)

$$c_{i,j,k,M} = c_{i,r,k,M} \ \forall \ i \in \mathcal{I}, \ j \in \mathcal{J}_2, \ k \in \mathcal{K}, \ l \in \mathcal{L}$$

$$(9)$$

Equations 10 and 11 model the recycle between successive stages and ensures that the correct flow rate and concentration values are fed back to the prior stage.

$$\sum_{l} q_{rd,k,l} = q_{re,k+1,M} \ \forall \ k \in \mathcal{K} \backslash N, \ l \in \mathcal{L}$$
 (10)

$$c_{i,rd,k,l} = c_{i,re,k+1,M} \ \forall \ i \in \mathcal{I}, \ k \in \mathcal{K} \backslash N, \ l \in \mathcal{L}$$
 (11)

Equation 12 arises from the fact that there can be no recycle streams entering the last membrane stage as there are no future stages. Likewise, the recycle leaving the first stage is set to zero in eq 13 as there are no prior stages.

$$q_{rd,N,l} = 0 \quad \forall \ l \in \mathcal{L} \tag{12}$$

$$q_{re,1,M} = 0 \tag{13}$$

Connectivity between elements of the same stage on the feed side is modeled using eqs 14 and 15 by linking the retentate and stage feed flow rates and concentration values.

$$q_{sf,k,l+1} = q_{r,k,l} \quad \forall \ k \in \mathcal{K}, \ l \in \mathcal{L}$$
 (14)

$$c_{i,sf,k,l+1} = c_{i,r,k,l} \quad \forall \ i \in \mathcal{I}, \ k \in \mathcal{K}, \ l \in \mathcal{L}$$

$$\tag{15}$$

Cascading between stages is realized by allowing the permeate leaving the last element to enter as stage feed to the first element of the next stage, modeled using eqs 16 and 17.

$$q_{sf,k+1,1} = q_{p,k,M} \quad \forall \ k \in \mathcal{K}$$
 (16)

$$c_{i,f,k+1,1} = c_{i,p,k,M} \quad \forall \ i \in \mathcal{I}, \ k \in \mathcal{K}$$
 (17)

The stage feed to the first element of the first stage of the cascade is set to zero in eq 18.

$$q_{f,1,1} = 0 (18)$$

Equations 19 and 20 model the overall and individual component material balances on the permeate side of the stage for each element.

$$q_{p,k,l+1} = q_{fl,k,l+1} + q_{p,k,l} \ \forall \ k \in \mathcal{K}, \ l \in \mathcal{L}$$
 (19)

$$\begin{aligned} q_{p,k,l+1} \times c_{i,p,k,l+1} &= q_{fl,k,l+1} \times c_{i,fl,k,l+1} + q_{p,k,l} \times c_{i,p,k,l} \\ \forall i \in I, \ k \in \mathcal{K}, \ l \in \mathcal{L} \end{aligned} \tag{20}$$

Equation 21 states that the flux (flow rate) through the first membrane element is equal to the permeate flow rate for that element.

$$q_{p,k,1} = q_{fl,k,1} \quad \forall \ k \in \mathcal{K}$$
 (21)

Equation 22 states that the average concentration of the streams entering the first membrane element must be equal to the permeate concentration of that element.

$$c_{i,p,k,1} = c_{i,fl,k,1} \quad \forall \ i \in \mathcal{I}, \ k \in \mathcal{K}$$
(22)

*Transport Constraints*. The next part of the model includes the governing transport equations that describe the performance of the membrane. Transport characteristics of the membrane are derived from differential material balances.

Equation 23 governs the flux across the membrane.

$$q_{fl,k,l} = \frac{J_{w} \times L_{k} \times w}{M} \quad \forall \ k \in \mathcal{K}, \ l \in \mathcal{L}$$
(23)

Equation 24 captures the concentration profile in the system. A log transformation is used in eq 24 to improve numeric conditioning. This transport model uses a lumped parameter model.

$$\begin{split} \log(c_{i,r,k,l}) + (S_i - 1) \times \log(q_{f,k,l}) &= \log(c_{i,f,k,l}) \\ + (S_i - 1) \times \log(q_{r,k,l}) \quad \forall \ i \in \mathcal{I}, \ k \in \mathcal{K}, \ l \in \mathcal{L} \end{split} \tag{24}$$

Equation 24 is the constraint that is directly impacted when analyzing alternative membrane properties. Most notably, the membrane selectivity  $\alpha = S_{\text{Li}^+}/S_{\text{Co}^{2+}}$  can be varied by adjusting the Li<sup>+</sup> or Co<sup>2+</sup> sieving coefficients (or both). These sieving coefficients are what are directly enter into eq 24.

*Product Recovery and Purity Constraints.* Equation 25 is the recovery of the permeate side product  $R_p$  (Li-rich solution).

$$R_{p} = \frac{q_{p,N,M} \times c_{1,p,N,M}}{Q_{ff} \times C_{1,ff} + Q_{fd} \times C_{1,fd}}$$
(25)

Equation 26 constrains the lithium recovery,  $R_p$ , to be at least as large as the parameter  $R^*$  as the cobalt recovery is maximized, which is the first optimization step. This is known as the  $\epsilon$ -constrained method for multiobjective optimization.

$$R_p \ge R^* \tag{26}$$

In a second optimization step (described below), the sum of the concentration of the impurities (I) in the lithium and cobalt product streams, defined by eq 27, is minimized.

$$c_{2,p,N,M} + \frac{\sum_{j} Q_{j} c_{1,j} - q_{p,N,M} \times c_{1,p,N,M}}{\sum_{j} Q_{j} - q_{p,N,M}} = I \ \forall j \in \mathcal{J}_{5}$$
(27)

The recovery of the retentate product  $R_r$  is modeled by eq 28. Modeling both  $R_p$  as well as  $R_r$  allows the maximization of the recovery of Li<sup>+</sup> or Co<sup>2+</sup> either by changing the objective function of the optimization problem or by adjusting the recovery parameter  $R^*$  in eq 26.

$$R_r = \sum_{j} Q_j c_{2,j} - q_{p,N,M} \times c_{2,p,N,M} \quad \forall j \in \mathcal{J}_5$$
(28)

For this study,  $\mathrm{Co^{2+}}$  recovery was typically maximized as it is the more valuable product. These recovery values were then fixed within a tolerance ( $\epsilon = 1 \times 10^{-4}$ ).

$$(1 - \epsilon)R_{p,\text{prior}} \le R_p \le (1 + \epsilon)R_{p,\text{prior}}$$
 (29)

$$(1 - \epsilon)R_{r,\text{prior}} \le R_r \le (1 + \epsilon)R_{r,\text{prior}}$$
 (30)

Stage cuts  $\theta$  (dimensionless) are defined by eq 31. The bounds on the stage cuts, eq 42, prevent any single membrane stage from becoming too large, which would result in subsequent stages of the cascade being starved of feed.

$$\theta_k \times \sum_{j,l} q_{j,k,l} + q_{sf,k,1} = q_{p,k,M} \quad \forall j \in \mathcal{J} \backslash sf, \ k \in \mathcal{K}, \ l \in \mathcal{L}$$

$$\tag{31}$$

Equation 32 calculates the overall membrane area  $A_{\rm m}$  (m<sup>2</sup>) across all stages required for a given process.

$$\sum_{k} L_{k} \times w = A_{m} \quad \forall \ k \in \mathcal{K}$$
(32)

Equation 33 is used for isotropic cascades, while eq 34 is used for anisotropic cascades.

$$L_k - l_{k+1} = 0 \quad \forall \ k \in \mathcal{K} \quad \text{(isotropic cascade)}$$
 (33)

$$L_k - l_{k+1} \ge 0 \quad \forall \ k \in \mathcal{K} \quad \text{(anisotropic cascade)}$$
 (34)

Bound Constraints. The bounds of the system ensure that any solution obtained is physically realizable. Equation 35 ensures that all flow rates are reasonable. The bounds on the flows prevent high recirculation rates in the system, which would incur uneconomically high piping and pumping costs. Additionally, bounding the recycle rate, eq 37, ensures that when anisotropic cascades are considered that the last stages within the cascade do not approach negligible values for their membrane area.

$$0 \le q_{i,k,l} \le \overline{q} \quad \forall j \in \mathcal{J}_l, \ k \in \mathcal{K}, \ l \in \mathcal{L}$$
(35)

$$0 \le q_{j,k,M} \le \overline{q} \quad \forall j \in \mathcal{J}_2, \ k \in \mathcal{K}$$
(36)

$$Re_{i,k,l} \le \overline{q_r} \quad \forall \ i \in I, \ k \in \mathcal{K}, \ l \in \mathcal{L}$$
 (37)

Equations 38 and 39 enforce the concentration solubility limits to prevent salt precipitation in the cascade.

$$0 \le c_{i,j,k,l} \le \overline{c_i} \quad \forall \ i \in I, \ j \in \mathcal{J}_l, \ k \in \mathcal{K}, \ l \in \mathcal{L}$$
(38)

$$0 \le c_{i,j,k,M} \le \overline{c_i} \quad \forall \ i \in I, \ j \in \mathcal{J}_2, \ k \in \mathcal{K}$$
(39)

Equations 40 and 41 ensure that no one stage is made too large and that a bounded amount of membrane area is used to accomplish the separation.

$$\underline{L} \le L_k \le \overline{L} \quad \forall \ k \in \mathcal{K} \tag{40}$$

$$A_{\rm m} \le A_{\rm m} \le \overline{A_{\rm m}} \tag{41}$$

Equation 42 ensures that no future stages are starved of feed in the cascade by ensuring that the stage cuts are finite.

$$\underline{\theta} \le \theta_k \le \overline{\theta} \quad \forall \ k \in \mathcal{K} \tag{42}$$

Equation 43 enforces that some minimum product is recovered.

$$R_r \ge \underline{R_{Co}} \tag{43}$$

**Multi-Objective Optimization Procedure.** We compute sets of Pareto optimal cascade designs that maximize both Co<sup>2+</sup> recovery and Li<sup>+</sup> recovery using a robust two-step optimization procedure, shown below, to help avoid local optimal solutions that are not practical. We first maximize Co<sup>2+</sup> recovery while constraining Li<sup>+</sup> recovery to be

above the threshold  $R^*$  as defined in eq 26. This is the classic epsilon-constrained method for multiobjective optimization. We record the solution, which concludes step 1. Next, in step 2, we add eqs 29 and 30 to ensure that the recovery of Li<sup>+</sup> and Co<sup>2+</sup> is at least as good as the step 1 solution (minus a small tolerance such as  $\epsilon = 10^{-4}$ ) and then minimize the impurities in the permeate and retentate products. We found that step 2 is necessary to reliably find physically sensible cascade designs. We hypothesize the step 1 objective, maximize Co<sup>2+</sup> recovery, is flat; i.e., there are many local solutions with nearly the same maximum Co<sup>2+</sup> recovery. Step 2 in the optimization procedure selects among these local solutions the design that minimizes impurities. We then repeat steps 1 and 2 while varying the Li<sup>+</sup> recovery threshold  $R^*$  in eq 26 to compute multiple Pareto optimal solutions, thus quantifying the tradeoff between Co<sup>2+</sup> recovery and Li<sup>+</sup> recovery for given membrane performance parameters and system specifications.

```
Step 1
maximize recovery retentate product, Eq. (28)
Li<sup>+</sup> recovery bounded Eq. (26)
Material balances, Eqs. (1)-(22)
Transport phenomena, Eqs. (23), (24)
Product recovery and impurity, Eqs. (25), (27)
System dimensions, Eqs. (31) and (32)
Isotropic/Anisotropic, Eq. (33)/(34)
Physical bounds, Eqs. (35)-(43)
Step 2
minimize impurities, Eq. (27)
Li<sup>+</sup> and Co<sup>2+</sup> recovery fixed, Eqs. (29), (30)
Material balances, Eqs. (1)-(22)
Transport phenomena, Eqs. (23) (24)
Product recovery, Eq. (25)
System dimensions, Eqs. (31) and (32)
Isotropic/Anisotropic, Eq. (33)/(34)
Physical bounds, Eqs. (35)-(43)
```

This two-step procedure was used to generate all of the sets of Pareto optimal solutions reported in the paper. This optimization procedure is fast and robust over a wide range of conditions. In each sensitivity analysis over the  $Li^+$  recovery threshold  $R^*$ , the prior solution was used to initialize the next optimization problem. If needed, this sensitivity analysis can be performed in reverse as well to find better locally optimal solutions. The entire initialization and optimization procedure requires less than 2 s per computed Pareto solution. (See the Figure 2 caption for additional computational timing results.) Alternatively, Li<sup>+</sup> recovery was held constant at 95%, and a sensitivity analysis was performed for the sieving coefficients in eq 24 to quantify the effect of varying membrane properties. Finally, to ensure that the design heuristics were not an artifact of the problem formulation, an alternate approach was considered; maximizing lithium recovery while perturbing a constraint on Co2+ recovery yielded very similar results as the optimization procedure described above.

#### ■ RESULTS AND DISCUSSION

Superstructure Optimization Model Captures Non-intuitive Trade-Offs. The superstructure optimization model illustrated in Figure 1 and defined in the Methods section is solved in terms of the percent of critical material recovered relative to that contained in the feed. As shown in Figure 2, Pareto optimal trade-offs were generated by solving the

superstructure optimization problem for many values of the Li<sup>+</sup> recovery. At each point, the amount of Co<sup>2+</sup> recovered was first maximized for a given Li+ recovery, and then the concentration of impurities in the product streams was minimized. For the solutions shown in Figure 2, all of the stages within the cascade are constrained to have the same amount of membrane area. Because of this constraint, these configurations are referred to as isotropic cascades. For these cascades, as you increase the number of stages, the Pareto trade-off shifts to higher recoveries, as shown in Figure 2A and Figure S1 in the Supporting Information. This increased recovery occurs at the cost of an increased membrane area budget, which is necessary to ensure finite stage cuts as shown in Figure S2. An additional benefit of increasing the number of stages is a steady improvement in the product purity as shown in Figure S3. With each added stage, there is the opportunity for Co<sup>2+</sup> that had permeated through the membrane in the penultimate stage to be recaptured in the retentate of the added stage resulting in a higher purity lithium product. In Figure 2 there are three sample designs shown at 25%, 60%, and 95% Li<sup>+</sup> recovery. These solutions reveal the variety of optimal designs that are elucidated. For example, as the amount of Li+ recovered is increased, the feed input stream progresses across the cascade, while the diafiltrate input location remains constant. Design II highlights that optimal designs may utilize nonintuitive approaches such as having a recycle stream enter in the middle of a stage rather than being fed to the beginning of the stage.

$$SF_{Li^{+}} = \frac{c_{Li^{+}}^{permeate}/c_{Co^{2+}}^{permeate}}{c_{Li^{+}}^{feed}/c_{Co^{2+}}^{feed}}, SF_{Co^{2+}} = \frac{c_{Co^{2+}}^{retentate}/c_{Li^{+}}^{retentate}}{c_{Co^{2+}}^{feed}/c_{Li^{+}}^{feed}}$$
(44)

Figure 3 further investigates these Pareto optimal designs by examining the purity and flow rate of the product streams as a function of Li<sup>+</sup> recovery. This additional analysis suggests that the Li<sup>+</sup> (permeate) separation factor is influenced more dramatically by design decisions (e.g., number of stages) than the Co<sup>2+</sup> (retentate) separation factor. The separation factor, defined in eq 44 as the ratio of the product concentration to the impurity concentration divided by the feed concentration ratio, allows the efficiency of the separation to be assessed on a normalized basis. The concentrations used to calculate the separation factors are shown in Figures S4, S5, and S6 for one-, three-, and five-stage system designs, respectively. For all values of Li<sup>+</sup> recovery, the Li<sup>+</sup> separation factor increases noticeably with the addition of each stage. The improved separation occurs as each additional stage provides another opportunity for lithium to permeate through the membrane while cobalt is retained. In contrast, the Co<sup>2+</sup> separation factor exhibits modest increases with the addition of more stages because the cobalt product is recovered as the retentate stream from the first stage. This design feature results in the Co<sup>2+</sup> separation factor depending more strongly on the Co<sup>2+</sup> sieving coefficient rather than the design complexity. Consistent with intuiation, as the Li<sup>+</sup> recovery increases, the Li<sup>+</sup> product flow rate increases, and the Co<sup>2+</sup> product flow rate decreases.

The proposed diafiltration designs offer an efficient means to fractionate a majority of the Li<sup>+</sup> and Co<sup>2+</sup> in the feed. Benchmarks for product purity vary widely in the literature from 95% Co purity<sup>81</sup> to greater than 99.5% Li purity.<sup>82</sup> In the context of LIB recycling, the proposed diafiltration designs would likely be followed with additional polishing steps to recover high-purity products, e.g., lithium carbonate, that are

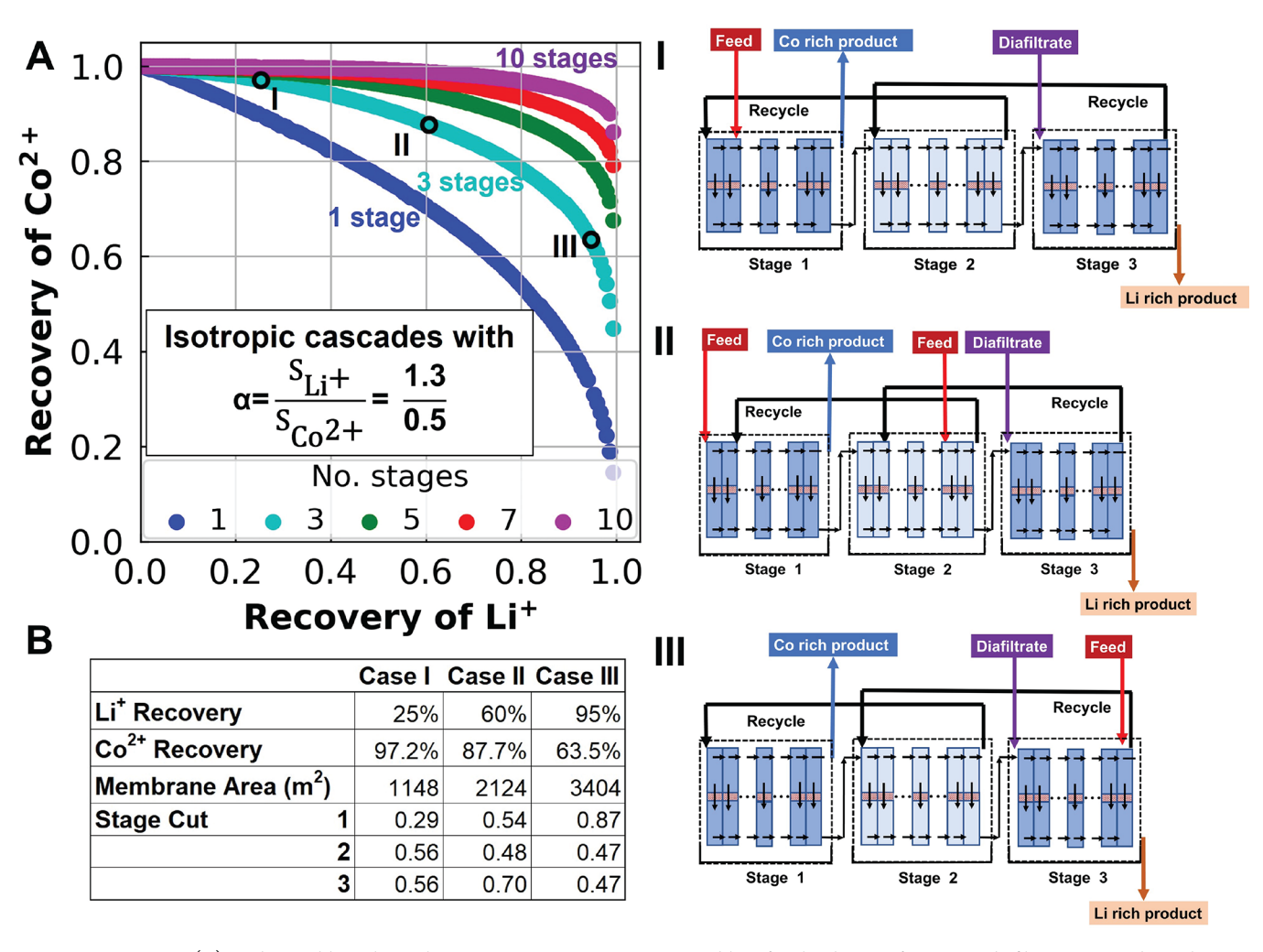


Figure 2. Pareto set (A) is obtained by solving the superstructure optimization problem for the design of isotropic diafiltration cascades utilizing a membrane with selectivity  $\alpha=2.6.^{79,80}$  Each point in the Pareto set, which represents a solution to the optimization problem and corresponds to a complete physical design for an isotropic cascade, was obtained by maximizing the  $\mathrm{Co}^{2+}$  recovery while constraining the  $\mathrm{Li}^+$  recovery to a specific value. Three representative three-stage configurations that highlight the heterogeneity of physical designs that can emerge with respect to recovery, membrane area, stage cut, and feed injection strategy are described in panel B and panels I–III. Design (I) at 25%  $\mathrm{Li}^+$  recovery has all the feed entering the first stage of the cascade. Design (II) at 60%  $\mathrm{Li}^+$  recovery has a split feed. Design (III) at 95%  $\mathrm{Li}^+$  recovery has the feed entering the last stage of the cascade. These three designs reveal a nonintuitive relationship between the targeted  $\mathrm{Li}^+$  recovery and the optimal location of the feed stream. Calculating the 151 solutions for the three-stage Pareto set, from which the three illustrations are taken, took 1 min and 37 s, for an average time of 0.64 s to compute each optimal design.

used in battery manufacturing. Within this context, the identification of the more desirable designs in the Pareto sets shown in Figures 2, 3, S4, S5, and S6 depends on a variety of factors including the value of the products (currently, Co is 2 to 3 times more valuable than Li) and the impact of the diafiltration effluent compositions and flow rates on other unit operations. Detailed modeling to select the best diafiltration cascade design within an integrated LIB recycling process is left as future work. Instead, by analyzing the plethora of solutions generated using the superstructure optimization framework, we postulate design heuristics arising from these trade-offs to assist separation scientists and engineers in considering the complex decisions that arise when designing these cascades.

Design Heuristics for Optimal Performance Using Isotropic Cascades. We distill over 1000 Pareto optimal isotropic cascade designs into six heuristics to generate Pareto optimal designs. These rules address the two primary design degrees of freedom—how to size membrane modules in the cascade and where to locate fresh feed, diafiltrate, recycle, and

product streams in each stage. Similar to analogous shortcut methods to design other separation cascades (e.g., absorption, distillation), these rules help reduce the complexity of diafiltration system design without having to use mathematical optimization and may help expand diafiltration beyond niche separations.

First, the sensitivity analysis shown in Figure 2 was repeated for N=1 to N=10 stages with Li<sup>+</sup> recovery constrained to at least 5% and 99%, resulting in a library of over 1000 Pareto optimal designs. Equality constraints were used to ensure equal membrane area across each stage. Visualizations including Figure 4 and video animations (MP4-1, MP4-2, MP4-3, MP4-4) in the Supporting Information reveal how the designs depend on the Li<sup>+</sup> recovery and the number of stages. Supporting data analysis and physical justification are provided below for each heuristic.

Design Heuristic 1: Product Stream Locations Maximize Usable Membrane Area. Independent of enforced Li<sup>+</sup> recovery, the cobalt (retentate) product stream is always removed from

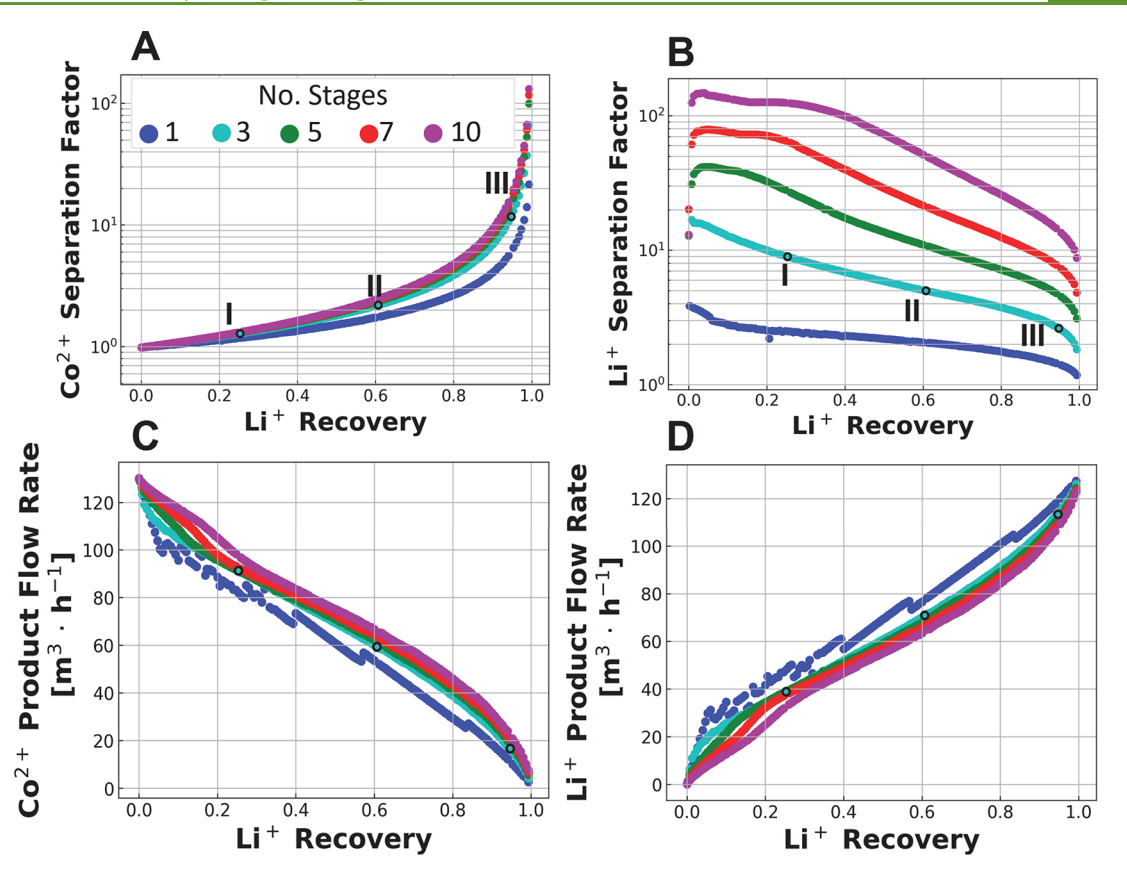


Figure 3. For the isotropic diafiltration cascade in Pareto set (A) of Figure 2, the  $Co^{2+}$  and  $Li^{+}$  separation factor is plotted in panels A and B for the  $Co^{2+}$  retentate product stream and the  $Li^{+}$  permeate product stream, respectively. The corresponding flow rates of these two product streams are shown in panels (C) and (D).

the first stage, and the lithium (permeate) product is always removed in the final stage. This configuration maximizes the usable membrane area in the cascade. It provides the greatest time (i.e., membrane area) for the preferential transport of lithium through the membrane, which produces higher quality Li-enriched permeate and Co-enriched retentate streams. When designing distillation columns for binary separations, the distillate and bottoms products are removed from opposite ends of the column for similar reasons. Agarwal draws a similar parallel between membrane and distillation cascades for multicomponent separations. <sup>83</sup>

Design Heuristic 2: Optimal Location of Fresh Diafiltrate Minimizes Lost Retentate Product. The diafiltrate enters the first elements of the last stage as highlighted by the blue points, which form a horizontal line in Figure 4. This rule is independent of Li<sup>+</sup> recovery, the number of stages in a cascade, or how this optimization problem is formulated. Physically, the heuristic arises because the Li-rich product is extracted as the permeate from the last stage, and any Co<sup>2+</sup> contained in this stream cannot be recovered. Therefore, for the maximal amount of cobalt to be retained and recycled back into the cascade, the diafiltrate is supplied to reduce the local Co<sup>2+</sup> concentration. The smaller driving force for permeation that results limits the undesired flux of cobalt through the membrane. Adding the diafiltrate prematurely may even "wash away" some of the retentate product by decreasing the concentration of cobalt where it is intended to be enriched. This finding is robust as the diafiltrate input location was not enforced through bounds or constraints. Moreover, as detailed in the Methods section, the same results

were found if the reverse optimization problem was solved and Li<sup>+</sup> recovery was maximized for a specific Co<sup>2+</sup> recovery.

Design Heuristic 3: Diafiltrate Flow Rate Controls Local Solute Concentration. At a fixed value of Li<sup>+</sup> recovery, increasing the diafiltrate flow rate increases the recovery of Co<sup>2+</sup> as seen in Figure S7. The additional diafiltrate flow reduces the concentration of Co<sup>2+</sup> within the system, which as highlighted above, improves the recovery of Co<sup>2+</sup> by limiting its transport through the membrane. However, Figure S9 shows this increased recovery comes at the cost of an increased membrane area for a fixed number of stages. Larger systems with more membrane area are needed to manage the additional fluid flowing through the system.

Thus, this analysis reveals an important trade-off between the diafiltrate flow rate, membrane area, number of stages, and separation performance. In regions where water is plentiful and cheap, the diafiltrate flow rate may be increased to achieve a given separation performance with fewer numbers of stages, reducing operational complexity. Depending on the design specifics, increasing the diafiltrate flow rate may either increase (larger area) or decrease (fewer pumps and skids) the capital costs and should increase the operating costs (pumping energy). However, if water is a constrained resource, the system can be adapted for these regions through the inclusion of more stages. To emphasize this point, Figure S8 shows the trade-off between Co<sup>2+</sup> impurity and Li<sup>+</sup> recovery at several diafiltrate flow rates. A key finding here is that, moving from 0 to 100 m<sup>3</sup> h<sup>-1</sup> diafiltrate flow rate, the Co<sup>2+</sup> permeate impurity decreases by almost 1 order of magnitude in a three-stage system. More than half of the benefits are realized moving from 0 to 50 m<sup>3</sup> h<sup>-1</sup> diafiltrate flow

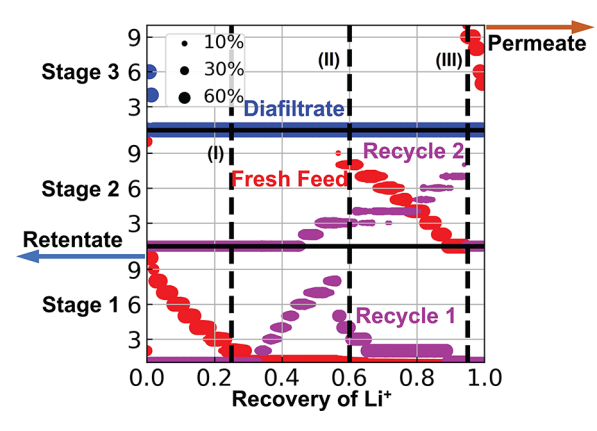


Figure 4. Optimal inlet locations of the feed (red circles), recycle to previous stage (pink circles), and diafiltrate (blue circles) streams for 151 different isotropic three-stage diafiltration designs are compared. Li<sup>+</sup> recovery, which was held constant during the solution of the optimization problem, is plotted on the horizontal axis. The vertical axis represents the length of a cascade; stage 1 starts at the bottom, and stage 3 ends at the top. The solid black lines divide the vertical axis to indicate the start of each stage (i.e., element 1). The horizontal gray gridlines demarcate select elements (i.e., elements 3, 6, and 9) within each stage, which were each modeled with 10 finite elements. Each vertical slice at fixed Li<sup>+</sup> recovery corresponds to an optimal solution with the location of the circles representing the injection locations of the various streams. If a stream enters at multiple locations, it is represented by multiple circles in the same vertical slice. As shown by the legend in the top left, the size of the circle denotes the fraction of the flow being injected at each location. The dashed vertical line corresponds to Designs I, II, and III marked in Figure 2, for 25%, 60%, and 95% Li<sup>+</sup> recovery, respectively. Note how, consistent with the schematics drawn in Figure 2, the feed injection locations (red circles) move from the beginning of stage 1 for Design (I), to a split feed for Design (II), and to the end of stage 3 for Design (III). In all the designs, the Co<sup>2+</sup>-rich retentate product is withdrawn at the end of stage 1 and the Li<sup>+</sup>-rich permeate product is withdrawn at the end of stage 3, as shown by the blue and orange arrows, respectively.

rate, which underscores the potential effectiveness of diafiltration systems even in water-constrained regions.

Design Heuristic 4: Fresh Feed Moves Across Cascade to Control Path Length to Final Product Stream Destination. The location of the feed stream is the primary variable controlling the relative amount of the two solutes recovered. In particular, the feed location determines the path length a solute travels from where it enters the cascade to where it exits in a product stream. Longer path lengths reduce solute recovery by increasing the probability of a solute being lost. The red curve in Figure 4 demonstrates the relationship between the location of the fresh feed and Li<sup>+</sup> recovery. At low Li<sup>+</sup> recovery (and high Co<sup>2+</sup> recovery), the feed enters the first stage. Then, as the amount of Li<sup>+</sup> recovered increases, the feed stream progresses along the cascade until at high Li<sup>+</sup> recovery the feed enters the last stage. As this progression of feed across the cascade occurs, the path length for lithium ions is reduced, while that for cobalt ions expands. This observation underpins the trade-off between Li<sup>+</sup> and Co<sup>2+</sup> recovery observed in the Pareto sets shown in Figure 2.

The concept of the path length is reinforced by examining the trend when the fresh feed moves from stage i to i+1. Namely, the feed moves to the far end of the new stage so that the additional membrane area is added to the path incrementally instead of through discrete quantities. For example, in Figure 4 at  $\sim$ 55% Li<sup>+</sup> recovery, the fresh feed moves to the end of the

second stage. In this way, the feed moves across the membrane area continuously as if it were unrolled linearly. These same patterns relating feed location to Li<sup>+</sup> recovery emerge for larger cascades, as demonstrated in Figure S10.

Design Heuristic 5: Optimal Mixing Dictates Recycle Feed Strategy. As noted above, the optimal feed location moves to maximize the recovery of the desired product. In tandem, the optimal location of the recycle streams moves to minimize the generation of entropy. This goal is accomplished by having the recycle streams enter the element of the prior stage that contains the retentate whose composition most closely matches theirs. The importance of matching concentrations is further bolstered by the fact that the feed does not progress along the cascade until the concentration of the subsequent stage reaches that of the fresh feed. The interconnected relationship between the optimal feed and recycle locations is demonstrated in Figure 4 where the red and purple lines correspond to the optimal feed, recycle to stage 1, and recycle to stage 2 streams, respectively. As Li+ recovery increases, the fresh feed progresses across stage 1; however, before it fully transitions to stage 2, the recycle stream to stage 1 moves toward the middle elements of stage 1. The maximum distance moved by the recycle occurs right before the feed transitions to stage 2. After this transition occurs, the recycle stream to stage 1 moves back toward the leading edge of stage 1. In the three-stage design captured in Figure 4, stage 2 is the penultimate stage. As such, it follows a different trend as there is no recycle being fed back into the last stage. These profiles, which are also observed for many stage systems (Figure S10), may appear chaotic at first glance but are moving in response to the changing concentration of lithium throughout the cascade. By moving across the stages in unison, the stream locations lead to small concentration differences that reduce the entropy of mixing allowing performance to be boosted holistically by the advantages of staging.

Design Heuristic 6: Splitting of Fresh Feed Enables Isotropic Cascade Designs. A split feed stream is needed to manage the flow of solution in systems with a higher number of stages. As the number of stages increases, the area per stage decreases. Therefore, the feed is split to maintain a stage cut between the physical bounds of 0 and 1 while not placing too great of a demand on any single stage. This phenomenon is particularly noticeable for systems with four or more stages where the feed is often split among three consecutive stages. For all systems, regardless of the number of stages, the feed is split as its optimal location progresses along the cascade and transitions from one stage to the next. For example, as depicted in Design II of Figure 2, this splitting allows for the smooth progression of the feed along the cascade as discussed above in Design Heuristic 4.

Relaxation of the Superstructure Model Reveals Novel Optimal Anisotropic Cascades. Relaxing the constraint of an isotropic cascade leads to enhanced recoveries. In particular, it introduces N-1 additional degrees of freedom that allow the superstructure to consider anisotropic designs where the membrane area per stage varies along the cascade. A sensitivity analysis for these anisotropic cascades and three sample designs are provided in Figure 5, which illustrates that an additional heuristic, related to the optimal distribution of the membrane area, emerges due to the extra degrees of freedom.  $\mathrm{Co}^{2+}$  permeate impurity and membrane area versus  $\mathrm{Li}^+$  recovery are shown in Figures S11 and S12. In this construct, the membrane area and stage cut taper down in magnitude across the cascade from left to right. The first stage accomplishes the bulk of the

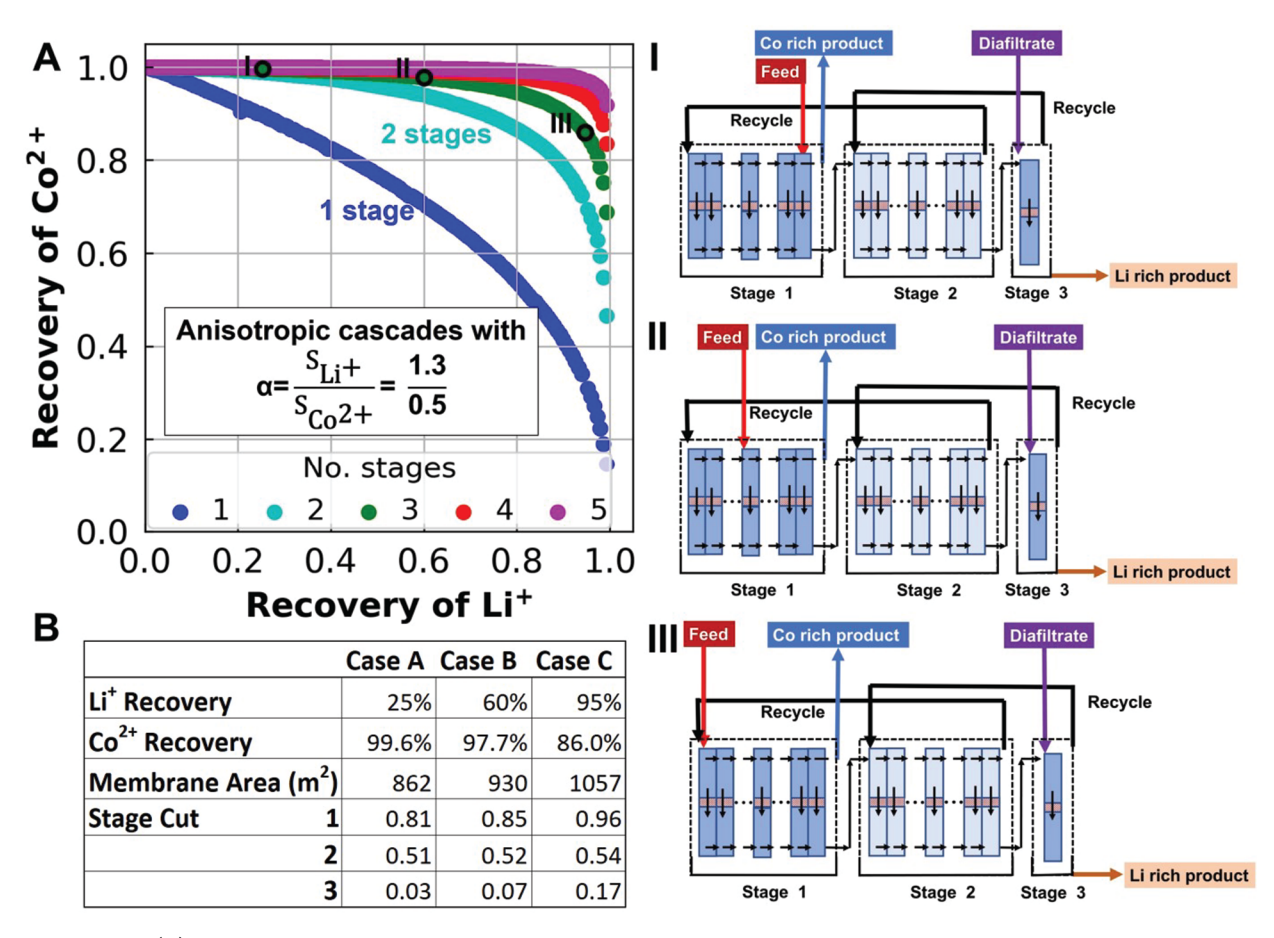


Figure 5. Pareto set (A) is obtained by solving the superstructure optimization problem for the design of anisotropic diafiltration cascades utilizing a membrane with selectivity  $\alpha=2.6$ . The flow rate of the recycle stream was bounded to a value of 500 m<sup>3</sup> h<sup>-1</sup>. Each point in the Pareto set is a solution for maximum  $\mathrm{Co^{2^{+}}}$  recovery subject to a specified  $\mathrm{Li^{+}}$  recovery. Moreover, each point on the plot is a complete physical design for an anisotropic cascade that can be realized using existing materials. <sup>79,80</sup> Three representative three-stage (N=3) configurations are described in panel B and panels I—III to highlight the heterogeneity of physical designs concerning their recoveries, membrane area, stage cuts, and feed injection strategies. Design (I) at 25%  $\mathrm{Li^{+}}$  recovery has the feed entering the right extreme of stage 1 of the cascade with the membrane area split 49%, 49%, and 2% across stages 1, 2, and 3, respectively. Design (II) at 60%  $\mathrm{Li^{+}}$  recovery has feed entering the middle of the first stage with the membrane area split 48%, 48%, and 4%. Design (III) at 95%  $\mathrm{Li^{+}}$  recovery has the feed entering the far left side of the first stage of the cascade with the membrane area split 46%, 46%, and 8%. These three designs reveal a significantly smaller final stage when compared to the preceding stages. Having a small final stage increases the recycle rate through the cascade, which enables an increased residence time for the feed and maximal utilization of membrane characteristics to recover higher quantities of  $\mathrm{Co^{2^{+}}}$  when compared with the isotropic cascade.

desired separation, while the subsequent stages are used for polishing the products. Less material can permeate through the smaller areas of the latter polishing stages thereby requiring more retentate to be returned to the prior stage as a recycle stream. In this way, the tapered design helps to mitigate the undesired permeation of Co2+ through the membrane and enhances recovery. The separation factors and flow rates for the Co<sup>2+</sup> and Li<sup>+</sup> product streams in Figure 6 reveal how these higher recoveries are achieved. Because the anisotropic designs can vary the membrane area in each stage, the system can more drastically change the product flow rates to help achieve higher recoveries relative to the more constrained isotropic cascades. Like what was seen in the isotropic cascades (Figure 3), the Co<sup>2+</sup> separation factor for anisotropic cascades is not strongly influenced by design considerations as it is mainly determined by the membrane's Co<sup>2+</sup> sieving coefficient. However, the Li<sup>2+</sup> separation factors for the anisotropic cascades are an order of magnitude higher than that for the isotropic cascades. Because this separation factor is dependent upon design decisions, increasing design complexity by adding degrees of freedom improves this separation factor relative to the more constrained

isotropic system. Detailed concentration plots for the product streams used to calculate the separation factor are given in Figures S13, S14, and S15 for a one-, three-, and five-stage anisotropic designs, respectively.

Impact of Anisotropic Cascades on Design Heuristics. The heuristics originally identified for isotropic cascades still hold for anisotropic cascades. As shown in Figure 7, the product streams exit at opposite ends of the cascade to maximize the total amount of usable membrane area, and the diafiltrate enters the last stage to minimize the amount of Co<sup>2+</sup> product lost. (Figure 7 caption further elaborates on this finding.) Additionally, Co<sup>2+</sup> recovery increases with the magnitude of the diafiltrate flow rate as this heuristic is related to the input to the whole system. The location of the fresh feed progresses across the cascade as the amount of Li<sup>+</sup> recovered increases. However, due to the size of the first stage, the concentration never reaches a value large enough for the feed to jump to the next stage. As such, the anisotropic cascade also follows the efficient mixing rules discussed above. Finally, in anisotropic cascades, the design decision regarding the optimal location of the feed is simplified because the first stage is large enough to obviate the need for splitting the feed.

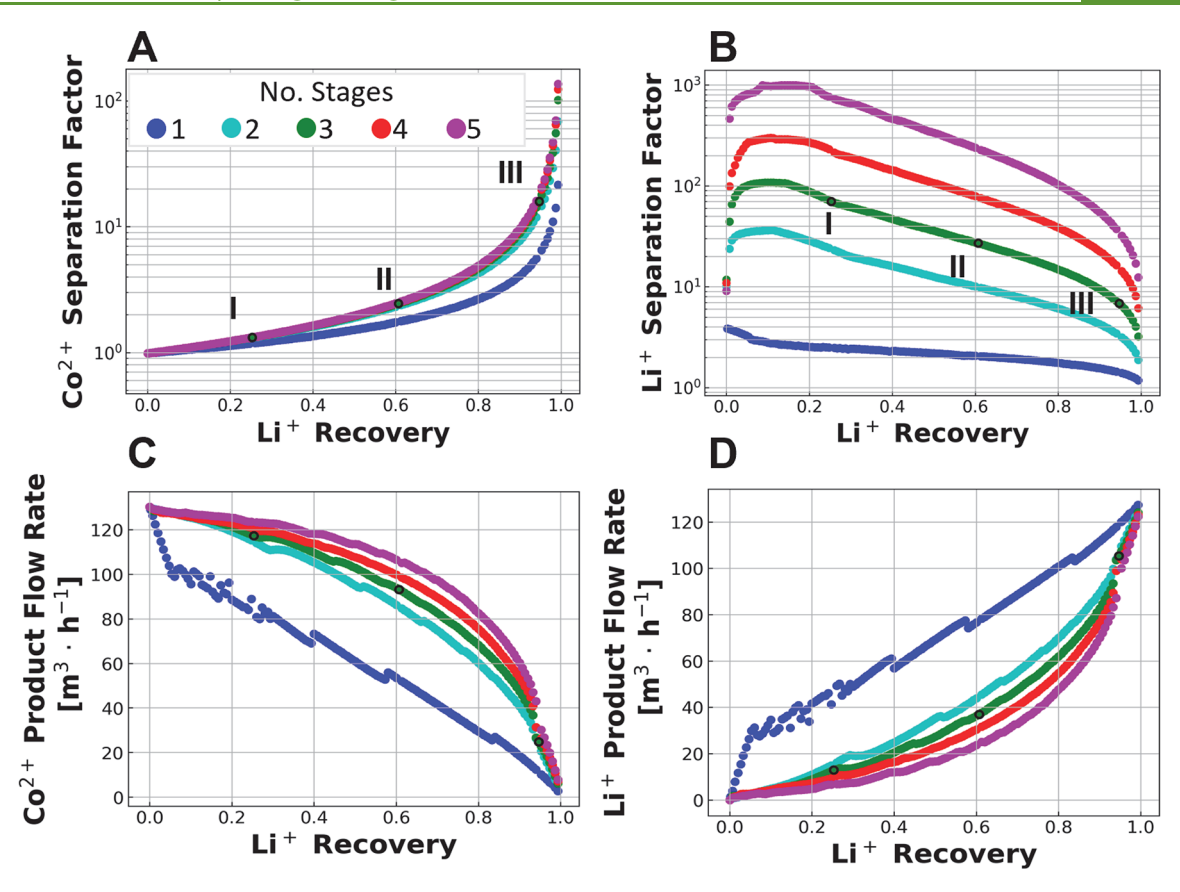


Figure 6. For the anisotropic diafiltration cascade in Pareto set (A) in Figure 5, the  $Co^{2+}$  and  $Li^{+}$  separation factor is plotted in panels (A) and (B) for the  $Co^{2+}$  retentate product stream and the  $Li^{+}$  permeate product stream, respectively. The corresponding flow rates of these two product streams are shown in panels (C) and (D).

However, as highlighted by Figure 7, the heuristics manifest in optimal flow patterns for the anisotropic systems that are rather simple in comparison to the flow patterns for the isotropic cascades (Figure 4). This simplicity arises due to the large size of the first stage and even simplifies the stage cuts for the system. In an anisotropic cascade, the first stage cut is the largest to permeate the most lithium through the cascade, whereas the stage cut is the smallest in the last stage to minimize the amount of cobalt pushed across the membrane. For an isotropic cascade, however, the stage cuts are much more complex as the system has N-1 fewer degrees of freedom due to the constraints that enforce all of the stages to have the same area. These stage cuts then vary to ensure that the flow rates balance for each stage. The complexity in the variation of the stage cuts reveal the necessity for such a framework as used in this paper. These stage cuts are reported in Figures S16 and S17.

Advantages of Anisotropic Cascades. A comparison of the anisotropic and isotropic designs reveals the complex trade-offs that the superstructure formulation allows process engineers to consider when attempting to customize a system to their unique needs. For example, Figure 8 demonstrates that a 10-stage isotropic cascade and a 4-stage anisotropic design perform comparably with regard to the recovery of critical materials. As such, the optimal design will depend on additional factors such as the relevant capital and operating costs. While the performance of the two designs is similar, the 10-stage isotropic system takes better advantage of the benefits that come from staging and thus requires only half the membrane area as the 4-stage anisotropic cascade (Figure 8). If anisotropic cascades are forced to use the same amount of membrane area as the

corresponding isotropic cascade, there is no significant advantage as shown in Figures S18 and S19. However, this reduced area may be offset by the cost associated with the six pumps needed to accommodate the additional stages. Another metric that may counteract the larger membrane area demands of anisotropic systems is the reduced diafiltrate demand. As mentioned above, the recycle flow rates are increased by the limited flux through the polishing stages of anisotropic designs. As such, the performance of anisotropic systems depends less on the amount of fresh diafiltrate utilized because the recycle streams serve as a proxy for the fresh diafiltrate. This finding is crucial if these anisotropic cascades are to be incorporated in areas where access to water is limited. Nonetheless, these two examples reveal the sheer customizability that this model gives to an engineer as there are thousands of different optimal solutions that have been found and can be adapted for many situations.

One of the main concerns in the past in realizing multistaged diafiltration membrane cascades is designing a cost-effective control system. Each additional stage adds another control loop, which causes the complexity to grow exponentially. Additionally, these membrane cascades can take a long time to reach steady state. Having trouble reaching steady state could be an issue if the system is shut down frequently for maintenance to replace fouled or scaled membrane modules. However, by using an anisotropic cascade, the maximal amount of membrane area can be used in the fewest number of stages, which simplifies the control problem. Also, cascades, in general, were shown to be more robust to fouling and may not need to be replaced as often since a cascade is shown to be able to maintain similar

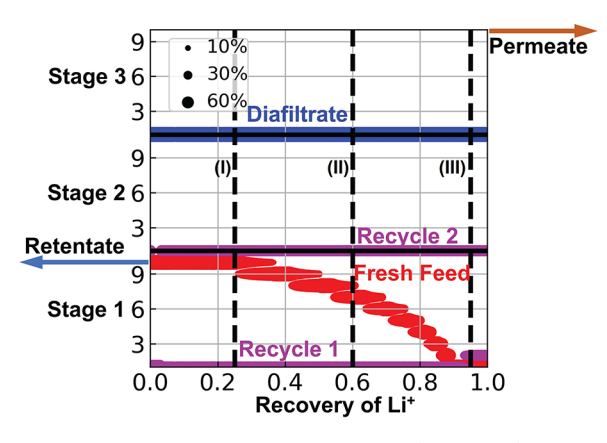


Figure 7. Optimal inlet locations of the feed (red circles), recycle to previous stage (pink circles), and diafiltrate (blue circles) streams for 151 different anisotropic three-stage diafiltration designs are compared. The horizontal axis plots the Li+ recovery, which was held constant during the solution of the optimization problem. The length of a cascade is represented by the vertical axis; stage 1 starts at the bottom, and stage 3 ends at the top. The solid black lines divide the vertical axis to indicate the start of each stage at element 1. The horizontal gray gridlines demarcate elements 3, 6, and 9 within each stage, which were each modeled with 10 elements. Each vertical slice at fixed Li<sup>+</sup> recovery corresponds to an optimal solution with the location of the circles representing the injection locations of the various streams. If a stream enters at multiple locations, it is represented by multiple circles in the same vertical slice. As shown by the legend in the top left, the size of the circle denotes the fraction of the flow being injected at each location. The dashed vertical lines correspond to Designs I, II, and III marked in Figure 5, for 25%, 60%, and 95% Li<sup>+</sup> recovery, respectively. Note how, consistent with the cascade schematics in Figure 5, the feed injection locations (red circles) move from the end of stage 1 for Design (I), toward the middle of stage 1 for Design (II), and the beginning of stage 1 for Design (III). In all the designs, the Co<sup>2+</sup>-rich retentate product is withdrawn at the end of stage 1, and the Li+-rich permeate product is withdrawn at the end of stage 3, as shown by the blue and tan arrows, respectively. For the solutions plotted, diafiltrate was constrained to be injected only into the last stage to prevent diluting the products. We hypothesize the dilution of the product with diafiltrate is an artifact of poor numerical scaling when trying to minimize product impurities at extreme recoveries. Similarly, we observed a spurious feed injection into element 1 of stage 3 at 100% Li+ recovery. This point is not shown as we believe it is also an artifact of poor numerical scaling.

performance standards even while the rejection ratio, or rather the performance of individual stages, was decreasing.<sup>84</sup>

Superstructure Optimization Quantifies Trade-Offs that Inform the Design of High Selectivity Materials. The flexibility of the superstructure model allows it to systematically explore the vast design space associated with the development of higher selectivity membranes. For example, Figure 9 shows nanofiltration membranes ( $\alpha = 10-30$ ) can improve recoveries of both species using less membrane area when compared to low selectivity membranes ( $\alpha = 2.6$ ). (The selectivity  $\alpha$  is a key membrane performance parameter in the optimization models described in the Methods.) Because of the smaller module size required, these membranes simplify the design of the system significantly when compared to a poor selectivity membrane. Nanofiltration membranes deployed in optimized diafiltration cascades, as shown in Figure 9, achieve fractionation efficiencies comparable with or in excess of current LIB recycling technologies without using organic solvents for liquid-liquid extraction<sup>62</sup> or ligands for chemical deposition.<sup>80</sup> Most importantly, these results suggest that this separation is

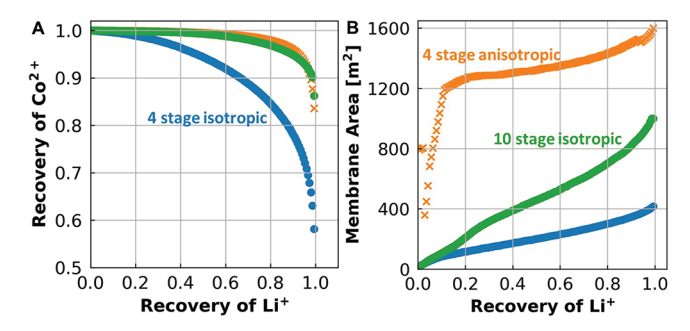


Figure 8. Performance comparison of isotropic and anisotropic diafiltration cascades. In both plots, circles indicate Pareto optimal isotropic designs, with the green and blue markers indicating 4- and 10stage configurations, respectively. The orange X's indicate optimal fourstage anisotropic cascades. (A) (left) Pareto curves highlighting the trade-offs between  $Co^{2+}$  and  $Li^+$  recovery. (B) (right) Membrane area requirement for Pareto optimal solutions. From a solute recovery perspective, the performance of the 4-stage anisotropic cascade is comparable with the 10-stage isotropic configuration. However, the 4stage anisotropic configuration has a higher membrane requirement when compared with the 10-stage isotropic cascade but provides favorable design options with less staging complexity. We hypothesize the solutions at Li<sup>+</sup> recovery less than 0.05 with membrane area near 800 m<sup>2</sup> indicate the presence of multiple local optima. Moreover, the membrane area is not penalized in the presented optimization formulation.

systems and device limited, instead of materials limited, as several current materials meet or exceed the selectivity target established by the superstructure framework.

To further elaborate on the nuanced trade-offs between selectivity, membrane area, recovery, purity, and system complexity, the table in Figure 9 compares the separation performance of nanofiltration membranes ( $\alpha = 10$ ) and lower selectivity membranes ( $\alpha = 2.6$ ) in the context of optimized systems. For example, the bottom two rows of the table show how staging reduces the need for high-performance materials. A two-stage isotropic diafiltration cascade utilizing a membrane with selectivity  $\alpha = 32$  requires 1536 m<sup>2</sup> of material to recover 99% Co<sup>2+</sup> and 95% Li<sup>+</sup>. In contrast, a single-stage separation will require a membrane with an order of magnitude higher selectivity  $\alpha = 311$  to achieve the same recovery. This higher selectivity requires an order of magnitude less membrane area (163 m<sup>2</sup>). If a three-stage isotropic cascade design is used, the same separation can be achieved using existing nanofiltration membranes with selectivity  $\alpha = 10$  and a 3648 m<sup>2</sup> of membrane area. Membranes with lower values of selectivity  $\alpha$  also achieve comparable performance in anisotropic cascades as shown by design (A) in Figure 9. Figures S20-S22 further compare recovery, impurity, and area trade-offs for different selectivity

Material Performance Targets for Next-Generation Membranes. As materials design continues to advance, the superstructure model can assist in identifying what level of membrane performance is necessary to achieve target metrics for Li<sup>+</sup> recovery and purity. Specifically, selectivity can be quantified using the ratio of the sieving coefficient of Li<sup>+</sup> to the sieving coefficient of  $\mathrm{Co^{2+}}$ ,  $\alpha = S_{\mathrm{Li^{+}}}/S_{\mathrm{Co^{2+}}}$ . As such, higher selectivity can be achieved by making a membrane less permeable to  $\mathrm{Co^{2+}}$  (i.e., reduce  $S_{\mathrm{Co^{2+}}}$ ), making a membrane more permeable to Li<sup>+</sup> (i.e., increase  $S_{\mathrm{Li^{+}}}$ ), or a combination thereof. In turn, distinct optimal system designs arise, even for membranes that exhibit the same selectivity, depending upon the approach used to

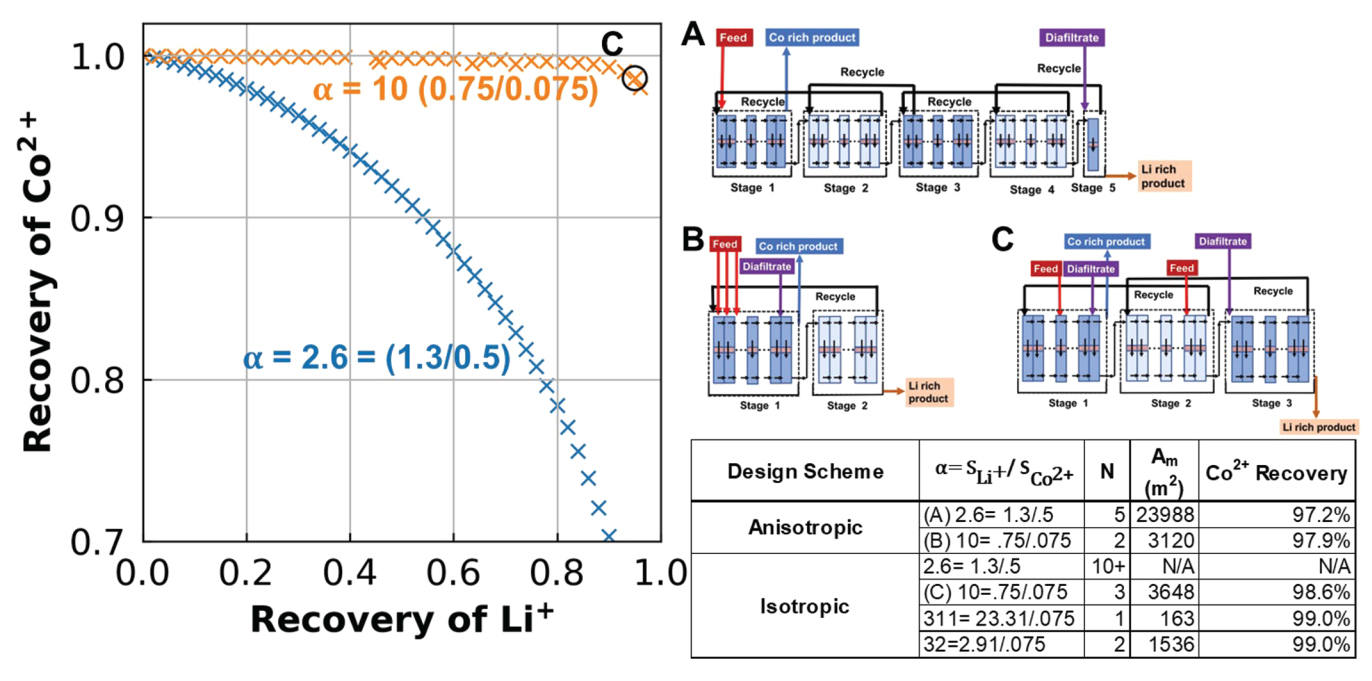


Figure 9. Graph on the left compares nanofiltration ( $\alpha$  = 10, orange) and a lower selectivity ( $\alpha$  = 2.6, blue) membrane deployed in optimized three-stage isotropic diafiltration cascades. The upper right corner of the plot (marked C) shows that the improved selectivity of the nanofiltration membranes enables diafiltration cascades to achieve 98.6%  $Co^{2+}$  recovery with 95%  $Li^+$  recovery. To further show the benefits of staging, several cascade designs that achieve 95% recovery of  $Li^+$  are compared on the right and detailed in the table on the bottom right. Design A is a five-stage anisotropic cascade that uses 23,988 m<sup>2</sup> of low selectivity  $\alpha$  = 2.6 membrane to achieve 95%  $Li^+$  recovery. Note that isotropic diafiltration cascades that have 10 or more stages but use membranes with low selectivity (row 3 of the table) fail to achieve separation targets comparable to Design A, thus highlighting the advantage of anisotropic cascades. Design B is another anisotropic cascade that utilizes only two stages with 3120 m<sup>2</sup> of nanofiltration membrane to achieve separation targets similar to design A. Design C (marked on the plot) is an isotropic cascade that employs 3648 m<sup>2</sup> of nanofiltration membrane in a three-stage system to achieve 98.6% and 95%  $Co^{2+}$  and  $Li^+$  recoveries respectively. Designs B and C show that the diafiltrate is injected close to the point where the retentate product  $Co^{2+}$  is being extracted from the cascade. This is because the high rejection ratio of the nanofiltration membrane leads to high concentrations of  $Co^{2+}$ , which may lead to salt precipitation near the point where the retentate product is being extracted, but the addition of diafiltrate prevents this from occurring.

enhance selectivity. Figure S23 details how three membranes of equivalent selectivity can have different systems scale requirements and performance. The membrane with high Li<sup>+</sup> permeability can achieve comparable Co<sup>2+</sup> recovery using less membrane area due to the higher sieving coefficient for the permeate product. This system, however, will produce an effluent product that has a lower purity than the product produced by using a system designed around a membrane with a high Co<sup>2+</sup> rejection rate. While the ideal scenario would likely be to develop materials that exhibit a high rejection of Co<sup>2+</sup> and large Li<sup>+</sup> flux, this approach may be constrained by physical limitations such as those underpinning the permeability-selectivity trade-off. Nevertheless, as new materials are designed, the superstructure model allows these futuristic trade-offs to be considered in the context of an optimal systems design.

Importantly, the guidance offered in this paper is in the context of optimal systems designs, which as highlighted above can be dramatically different for membranes with comparable selectivity. A sensitivity analysis over the cobalt and lithium sieving coefficients was performed by holding the Li<sup>+</sup> recovery constant at 95% and maximizing the Co<sup>2+</sup> recovery. The resulting recovery of Co<sup>2+</sup> and purity of the lithium product, reported as the concentration of Co<sup>2+</sup> in the Li<sup>+</sup> permeate product, are plotted as a function of membrane selectivity in Figure 10. The top row achieves high selectivity by making the membrane progressively less permeable to Co<sup>2+</sup>, while the lithium sieving coefficient is held constant at 0.75. The bottom row holds the cobalt sieving coefficient constant at 0.075 while

increasing the lithium sieving coefficient. For this latter case, shown in Figure 10c,d, above a selectivity of 13.33, the lithium sieving coefficient becomes greater than 1, which implies that the membranes enriches the concentration of Li<sup>+</sup> in the permeate solution relative to the concentration of Li<sup>+</sup> in the retentate solution. While some nanofiltration membranes capable of increasing the concentration of dissolved ions have been developed, to date, none have been able to produce permeate concentration that are more than five times higher than the retentate concentration. Therefore, realizing increased selectivities using this approach may be a challenge. Furthermore, even if such membranes could be developed, a comparison with Figure 10a,b highlights that producing membranes with reduced Co sieving coefficients enable the designs of systems that generate higher purity products. Thus, understanding how the selectivity is achieved is crucial to understanding how materials property targets are established for next-generation membranes. Moreover, the results in Figure 10 show that if the system is constrained to a single stage, selectivity values greater than 100 are needed to realize 95% Li<sup>+</sup> and 99% Co<sup>2+</sup> recoveries. Thus, considering cascades with multiple stages can mitigate the need for difficult to engineering membrane materials.

The sensitivity analysis in Figure 10 also illustrates that advances in high selectivity materials will need to be paired with novel system designs to reach the recovery and purity targets necessary for recycling Li-ion batteries. For example, transitioning from a one-stage to a two-stage design results in an order of

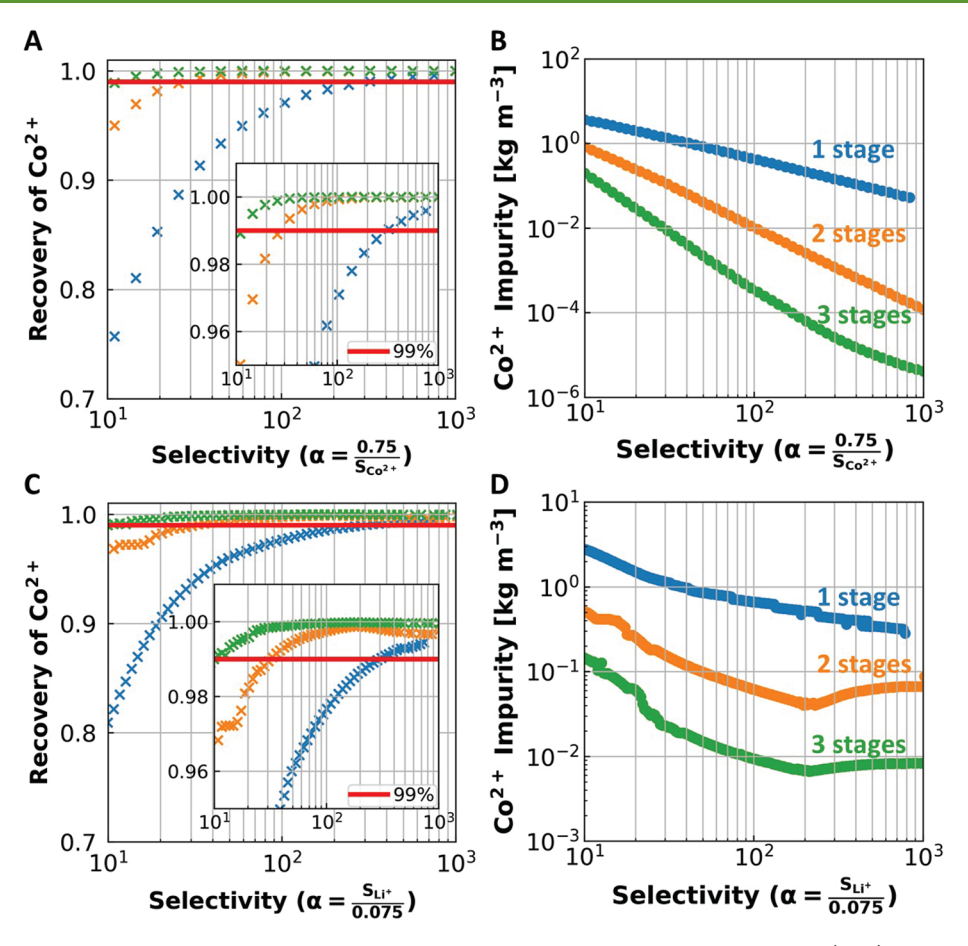


Figure 10. A sensitivity analysis was conducted over a range of membrane selectivities  $\alpha$  for a single-stage system (blue), a two-stage system (orange), and a three-stage system (green) holding the Li<sup>+</sup> recovery constant at 95%. The selectivity of the membranes was modulated in two different ways. The first row (panels A and B) reduces the cobalt sieving coefficient  $S_{\text{Co}^{2+}}$  while holding the lithium sieving coefficient constant ( $S_{\text{Li}^{+}} = 0.75$ ) to simulate the membrane rejecting more of the retained species, cobalt. The bottom row (panels C and D) was generated by holding the cobalt sieving coefficient constant at  $S_{\text{Co}^{2+}} = 0.075$  and varying  $S_{\text{Li}^{+}}$  to increase the Li<sup>+</sup> flux through the membrane. The red line indicates a benchmark value of 95% Li<sup>+</sup> recovery and 99% Co<sup>2+</sup> recovery. The point where the red line and Pareto set intersect corresponds to the membrane selectivity requirement for the benchmark process. These results emphasize the use of staging (systems design) to meet separation targets with materials of varying characteristics. For example, in panel A a single-stage system requires a membrane selectivity  $\alpha = 311$ , while the two-stage system only needs a selectivity  $\alpha = 32$  to achieve the benchmark metrics. If utilizing a three-stage system, the benchmark can be achieved using membranes with  $\alpha \approx 10$ . Panel C shows analogous benefits if  $S_{\text{Li}^{+}}$  is varied instead of  $S_{\text{Co}^{2+}}$  further highlighting that diafiltration cascades can achieve performance targets that cannot be achieved by single-stage systems. Comparing panels B and D, it is seen that the purity of Li<sup>+</sup> in the permeate product is notably higher if membranes that reject Co<sup>2+</sup> (top, B) are utilized rather than if membranes that are more permeable to Li<sup>+</sup> (bottom, D) are implemented. The presented results exemplify how the optimization framework provides quantitative guidance when developing new membranes with improved selectivity.

magnitude reduction in the selectivity needed to achieve a benchmark performance of 99% Co<sup>2+</sup> recovery and 95% Li<sup>+</sup> recovery. Notably, optimally designed two and three-stage cascades utilizing membranes with selectivities comparable to current nanofiltration materials,  $\alpha = 10-30$ , can achieve a similar performance as a single-stage system utilizing a highly selective membrane,  $\alpha$  > 100. Moreover, staging allows for the production of higher purity products, which are exceedingly difficult to accomplish in a single-stage fractionation step even when using highly selective membranes. The benefits of staging extend beyond product recovery and purity. The addition of the recycle streams increases the robustness of the system by keeping the concentration of solutes within the system lower, which helps to mitigate issues associated with scale formation. Thus, diafiltration is a systems solution to a materials problem that attains pure product while keeping both salts from precipitating out of the solution.

In summary, Figure 10 shows how different means to realize new materials with increased selectivity impact recoveries and impurities when said membranes are optimally deployed in a simulated industrial-scale separation. Through simultaneous process systems and material science engineering, this flexible framework can set benchmarks to guide future experiments. In addition to facilitating the recovery and enrichment of Co<sup>2+</sup> and Li<sup>+</sup>, the developed membranes will need to satisfy design criteria related to their stability, cost, and resilience to fouling, which can be informed by future extensions of the superstructure optimization framework.

Influence of Sieving Coefficients on Design Heuristics. As expected, increasing the selectivity ratio by perturbing the sieving coefficients will increase performance. This is because the value of the individual sieving coefficients informs how a system may be configured to accomplish the target separation. For a solute that is retained by the membrane (S < 1), the solute concentration in the retentate solution increases over the length

of the cascade. While the solute concentration in the retentate solution will decrease for a solute that preferentially permeates through the membrane (S > 1). This behavior can be observed in the Supporting Videos (MP4-1 to MP4-4) where the solute concentration profiles with percent recovery are reported for two cascades. The first cascade utilizes a membrane with  $\alpha = S_{\text{Li}^+}/S_{\text{Co}^{2+}} = 0.75/0.075$ , and the second cascade assumes a membrane with  $\alpha = S_{\rm Li^+}/S_{\rm Co^{2+}} = 1.3/0.5$ . Because of the different  $S_{Li^+}$  values, these two solutions exhibit Li<sup>+</sup> concentration profiles of opposite slopes. Therefore, to ensure the efficient mixing discussed in Design Heuristic 5, the input location of the recycle streams progress through the stages of these cascades in the opposite manner. The input stream for the  $S_{\text{Li}^+} = 0.75$  cascade then enters at the beginning of the cascade and moves to the end as the concentration of Li<sup>+</sup> is accumulating within the stage. The opposite pattern is shown for the  $S_{Li^+} = 1.3$  membrane as the Li<sup>+</sup> concentration decreases throughout the stage as seen in Figure 4.

Heuristics may be disregarded in some optimal designs to compensate for other physical constraints imposed upon the system. For example, if designing a cascade using a membrane with S < 1, careful consideration should be given to the solubility limit of the relevant salts. In these systems, the concentration within the retentate is lowest where the feed, recycle, and diafiltrate streams enter the cascade. This feature should be accounted for when determining the feed and recycle input locations since these streams can be used to dilute the solute concentration. The optimization framework detailed here does this automatically. For example, in Figure 9 the membrane used in Design B violates the heuristic that the fresh diafiltrate should enter the last stage. In this instance, the system needs to input the diafiltrate close to where the retentate Co<sup>2+</sup> product is being extracted to avoid the solubility constraint encoded within the superstructure model. Additionally, as shown in Designs B and C of Figure 9, the fresh feed is fed into the cascade at multiple locations to reduce the concentration of Co<sup>2+</sup> within the retentate across the cascade.

#### CONCLUSIONS AND OUTLOOK

The proposed superstructure model allows engineers to quickly quantify complex performance Pareto optimal trade-offs for diafiltration cascades. Diafiltration cascades can effectively leverage nanofiltration and high selectivity membranes by abating the main barrier to industry adoption, salt precipitation, through the optimized addition of diafiltrate. This superstructure model shows how systems-level analysis enables the comparison of advanced membrane materials for challenging separations including LIB recycling. The optimization analysis reveals that existing materials are already at property target goals that will allow them to compete with selective leaching technology and can even be used to benchmark future experiments. This materials-to-systems analysis is critical to realizing sustainable lithium recycling and reuse cycles that protect the environment and human health. Design heuristics are proposed to allow isotropic cascades to be quickly implemented within industry without rigorous mathematical optimization. These heuristics are greatly simplified for anisotropic cascades due to the additional degrees of freedom.

In the future, this framework is intended to be extended by considering both dynamic cascades and more complex separations with many ions. By looking at multicomponent separations, design heuristics will be proposed and compared to the standard design heuristics used in designing other separation cascades (e.g., distillation). Additionally, model predictive control should be explored to manage the dynamic operation of diafiltration cascades with a large number of stages. Likewise, these optimization results show the benefits of three or more stages and motivate experimental validation. Finally, structure—property—processing relationships and cost correlations can be incorporated into the superstructure to facilitate holistic molecular-to-systems optimization of diafiltration separations.

#### ASSOCIATED CONTENT

#### Supporting Information

The Supporting Information is available free of charge at https://pubs.acs.org/doi/10.1021/acssuschemeng.2c02862.

Supporting video 1: shows an isotropic cascade with the lithium sieving coefficient equal to 1 and thus has a flat Li<sup>+</sup> concentration profile (MP4-1)

Supporting video 2: shows a three-stage isotropic cascade, similar to Figure 2. The video reveals how the streams move as the amount of Li<sup>+</sup> recovered increases (MP4-2) Supporting video 3: shows how a nanofiltration cascade moves its input streams as a function of Li<sup>+</sup> recovery and shows how the diafiltrate is needed to counteract concentration gradients (MP4-3)

Supporting video 4: shows that the design heuristics proposed for an isotropic cascade hold for a higher number of stages. Notice how the feed is split across many stages for this cascade (MP4-4)

Supporting figures show additional trade-offs between recovery, purity, and stage cut (PDF)

#### **■** AUTHOR INFORMATION

#### **Corresponding Author**

Alexander W. Dowling — Department of Chemical and Biomolecular Engineering, University of Notre Dame, Notre Dame, Indiana 46556, United States; © orcid.org/0000-0001-9383-7499; Email: adowling@nd.edu

#### Authors

Noah P. Wamble — Department of Chemical and Biomolecular Engineering, University of Notre Dame, Notre Dame, Indiana 46556, United States; Occid.org/0000-0003-0769-727X

Elvis A. Eugene — Department of Chemical and Biomolecular Engineering, University of Notre Dame, Notre Dame, Indiana 46556, United States; orcid.org/0000-0003-2996-7031

William A. Phillip – Department of Chemical and Biomolecular Engineering, University of Notre Dame, Notre Dame, Indiana 46556, United States; orcid.org/0000-0001-8871-585X

Complete contact information is available at: https://pubs.acs.org/10.1021/acssuschemeng.2c02862

#### **Author Contributions**

E.A.E., W.A.P., and A.W.D. conceptualized the research with support from N.P.W.; E.A.E and N.P.W. created the optimization models and software (methods) with support from A.W.D.; N.P.W. and E.A.E analyzed and visualized the results with the support of W.A.P and A.W.D; all authors prepared the original draft and revised the manuscript.

#### **Author Contributions**

\*N.P.W. and E.A.E. contributed equally to this work.

#### Notes

The authors declare no competing financial interest.

#### ACKNOWLEDGMENTS

This work was primarily supported by the University of Notre Dame. N.P.W. gratefully acknowledges support from the Vincent P. Slatt Fellowship for Undergraduate Research in Energy Systems and Processes. E.A.E. gratefully acknowledges support from the Patrick and Jana Eilers Graduate Student Fellowship for Energy Related Research. Computational experiments were performed on the Notre Dame Center for Research Computing (CRC) high-performance computing cluster. A.W.D. and E.A.E. acknowledge partial support from the U.S. National Science Foundation Grant CBET-1941596. W.A.P. acknowledges partial support from the U.S. National Science Foundation Grant CMMI-1932206.

#### REFERENCES

- (1) Bohlsen, M. The Lithium Boom An Analysis of Future Demand vs. Supply. https://seekingalpha.com/article/3984654-lithium-boom-analysis-of-future-demand-vs-supply, 2016; Date of Access: July 1, 2021
- (2) Boudette, N.; Davenport, C. G.M. Will Sell Only Zero-Emission Vehicles by 2035. https://www.nytimes.com/2021/01/28/business/gm-zero-emission-vehicles.html, 2021; Date of Access: July 1, 2021.
- (3) Grafeo, E. Tesla's stock price surged 740% in 2020. Here's where 5 analysts say the shares are headed next. https://markets.businessinsider.com/news/stocks/tesla-stock-price-outlook-target-wall-street-analyst-goldman-jpmorgan-2020-12-1029928577, 2021; Date of Access: July 1, 2021
- (4) Sonoc, A.; Jeswiet, J.; Soo, V. K. Opportunities to Improve Recycling of Automotive Lithium Ion Batteries. *Procedia CIRP* **2015**, 29, 752–757. The 22nd CIRP Conference on Life Cycle Engineering.
- (5) Swain, B. Recovery and recycling of lithium: A review. Sep. Purif. Technol. 2017, 172, 388–403.
- (6) Kang, D. H. P.; Chen, M.; Ogunseitan, O. A. Potential Environmental and Human Health Impacts of Rechargeable Lithium Batteries in Electronic Waste. *Environ. Sci. Technol.* **2013**, 47, 5495–5503
- (7) Gaines, L. Lithium-ion battery recycling processes: Research towards a sustainable course. *Sustainable Materials and Technologies* **2018**, 17, No. e00068.
- (8) Morse, I. A Dead Battery Dilemma. Science 2021, 372, 780-783.
- (9) Ordoñez, J.; Gago, E.; Girard, A. Processes and technologies for the recycling and recovery of spent lithium-ion batteries. *Renewable & Sustainable Energy Reviews* **2016**, *60*, 195–205.
- (10) Harper, G.; Sommerville, R.; Kendrick, E.; Driscoll, L.; Slater, P.; Stolkin, R.; Walton, A.; Christensen, P.; Heidrich, O.; Lambert, S.; Abbott, A.; Ryder, K. S.; Gaines, L.; Anderson, P. Recycling lithium-ion batteries from electric vehicles. *Nature* **2019**, *575*, 75–86.
- (11) Costa, C.; Barbosa, J.; Gonçalves, R.; Castro, H.; Campo, F. D.; Lanceros-Méndez, S. Recycling and environmental issues of lithium-ion batteries: Advances, challenges and opportunities. *Energy Storage Materials* **2021**, *37*, 433–465.
- (12) Yang, Y.; Xu, S.; He, Y. Lithium recycling and cathode material regeneration from acid leach liquor of spent lithium-ion battery via facile co-extraction and co-precipitation processes. *Waste Management* **2017**, *64*, 219–227.
- (13) Chen, X.; Kang, D.; Cao, L.; Li, J.; Zhou, T.; Ma, H. Separation and recovery of valuable metals from spent lithium ion batteries: Simultaneous recovery of Li and Co in a single step. *Sep. Purif. Technol.* **2019**, *210*, *690*–*697*.
- (14) Jo, C.-H.; Myung, S.-T. Efficient recycling of valuable resources from discarded lithium-ion batteries. *J. Power Sources* **2019**, 426, 259–265.
- (15) Zhang, X.; Li, L.; Fan, E.; Xue, Q.; Bian, Y.; Wu, F.; Chen, R. Toward sustainable and systematic recycling of spent rechargeable batteries. *Chem. Soc. Rev.* **2018**, *47*, 7239–732.

- (16) Li, X.; Mo, Y.; Qing, W.; Shao, S.; Tang, C. Y.; Li, J. Membrane-based technologies for lithium recovery from water lithium resources: A review. *J. Membr. Sci.* **2019**, *591*, 117317.
- (17) Nightingale, E., Jr. Phenomenological theory of ion solvation. Effective radii of hydrated ions. *J. Phys. Chem.* **1959**, *63*, 1381–1387.
- (18) Razmjou, A.; Asadnia, M.; Hosseini, E.; Habibnejad Korayem, A.; Chen, V. Design principles of ion selective nanostructured membranes for the extraction of lithium ions. *Nat. Commun.* **2019**, *10*, 5793.
- (19) Sujanani, R.; Landsman, M. R.; Jiao, S.; Moon, J. D.; Shell, M. S.; Lawler, D. F.; Katz, L. E.; Freeman, B. D. Designing solute-tailored selectivity in membranes: perspectives for water reuse and resource recovery. *ACS Macro Lett.* **2020**, *9*, 1709–1717.
- (20) Alvarez, P. J.; Chan, C. K.; Elimelech, M.; Halas, N. J.; Villagrán, D. Emerging opportunities for nanotechnology to enhance water security. *Nat. Nanotechnol.* **2018**, *13*, 634–641.
- (21) Bae, H.; Kim, Y. Technologies of lithium recycling from waste lithium ion batteries: a review. *Materials advances* **2021**, *2*, 3234–325.
- (22) Li, X.; Mo, Y.; Qing, W.; Shao, S.; Tang, C. Y.; Li, J. Membrane-based technologies for lithium recovery from water lithium resources: A review. *J. Membr. Sci.* **2019**, *591*, 117317.
- (23) Luo, J.; Crittenden, J. C. Nanomaterial Adsorbent Design: From Bench Scale Tests to Engineering Design. *Environ. Sci. Technol.* **2019**, 53, 10537–10538.
- (24) Eugene, E. A.; Phillip, W. A.; Dowling, A. W. Data science-enabled molecular-to-systems engineering for sustainable water treatment. *Current Opinion in Chemical Engineering* **2019**, *26*, 122–130.
- (25) Eugene, E. A.; Phillip, W. A.; Dowling, A. W. Material Property Targets to Enable Adsorptive Water Treatment and Resource Recovery Systems. *ACS ES&T Engineering* **2021**, *1*, 1171–1182.
- (26) Blatt, W.; Robinson, S.; Bixler, H. J. Membrane ultrafiltration: the diafiltration technique and its application to microsolute exchange and binding phenomena. *Anal. Biochem.* **1968**, *26*, 151–173.
- (27) Ng, P.; Lundblad, J.; Mitra, G. Optimization of solute separation by diafiltration. *Sep. Sci. Technol.* **1976**, *11*, 499–502.
- (28) Strathmann, H. Selective removal of heavy metal ions from aqueous solutions by diafiltration of macromolecular complexes. *Sep. Sci. Technol.* **1980**, *15*, 1135–1152.
- (29) Richard Bowen, W.; Wahab Mohammad, A. Diafiltration by nanofiltration: prediction and optimization. *AIChE J.* **1998**, *44*, 1799–1812
- (30) Madsen, R. Design of sanitary and sterile UF- and diafiltration plants. *Sep. Purif. Technol.* **2001**, 22–23, 79–87.
- (31) Lipnizki, F.; Boelsmand, J.; Madsen, R. F. Concepts of industrial-scale diafiltration systems. *Desalination* **2002**, *144*, 179–184.
- (32) Sheth, J. P.; Qin, Y.; Sirkar, K. K.; Baltzis, B. C. Nanofiltration-based diafiltration process for solvent exchange in pharmaceutical manufacturing. *J. Membr. Sci.* **2003**, *211*, 251–261.
- (33) Ouimet, J. A.; Liu, X.; Brown, D. J.; Eugene, E. A.; Popps, T.; Muetzel, Z. W.; Dowling, A. W.; Phillip, W. A. DATA: Diafiltration Apparatus for high-Throughput Analysis. *J. Membr. Sci.* **2022**, *641*, 119743.
- (34) Kilmartin, C. P.; Ouimet, J. A.; Dowling, A. W.; Phillip, W. A. Staged Diafiltration Cascades Provide Opportunities to Execute Highly Selective Separations. *Ind. Eng. Chem. Res.* **2021**, *60*, 15706–15719.
- (35) Nambiar, A. M. K.; Li, Y.; Zydney, A. L. Countercurrent staged diafiltration for formulation of high value proteins. *Biotechnol. Bioeng.* **2018**, *115*, 139–144.
- (36) Dowling, A. W.; Biegler, L. T. A framework for efficient large scale equation-oriented flowsheet optimization. *Comput. Chem. Eng.* **2015**, 72, 3–20.
- (37) Mencarelli, L.; Chen, Q.; Pagot, A.; Grossmann, I. E. A review on superstructure optimization approaches in process system engineering. *Comput. Chem. Eng.* **2020**, *136*, 106808.
- (38) Chen, Q.; Grossmann, I. Recent developments and challenges in optimization-based process synthesis. *Annu. Rev. Chem. Biomol. Eng.* **2017**, *8*, 249–283.
- (39) Saif, Y.; Elkamel, A.; Pritzker, M. Superstructure optimization for the synthesis of chemical process flowsheets: application to optimal

- hybrid membrane systems. Engineering Optimization 2009, 41, 327–350.
- (40) Alnouri, S. Y.; Linke, P. A systematic approach to optimal membrane network synthesis for seawater desalination. *J. Membr. Sci.* **2012**, *417*, 96–112.
- (41) Karuppiah, R.; Bury, S. J.; Vazquez, A.; Poppe, G. Optimal design of reverse osmosis-based water treatment systems. *AIChE J.* **2012**, *58*, 2758–2769.
- (42) Khor, C. S.; Foo, D. C.; El-Halwagi, M. M.; Tan, R. R.; Shah, N. A superstructure optimization approach for membrane separation-based water regeneration network synthesis with detailed nonlinear mechanistic reverse osmosis model. *Ind. Eng. Chem. Res.* **2011**, *50*, 13444–13456.
- (43) Khor, C. S.; Chachuat, B.; Shah, N. A superstructure optimization approach for water network synthesis with membrane separation-based regenerators. *Comput. Chem. Eng.* **2012**, 42, 48–63.
- (44) Sassi, K. M.; Mujtaba, I. M. MINLP based superstructure optimization for boron removal during desalination by reverse osmosis. *J. Membr. Sci.* **2013**, 440, 29–39.
- (45) Buabeng-Baidoo, E.; Majozi, T. Effective synthesis and optimization framework for integrated water and membrane networks: a focus on reverse osmosis membranes. *Ind. Eng. Chem. Res.* **2015**, *54*, 9394–9406.
- (46) Abass, M.; Majozi, T. Optimization of integrated water and multiregenerator membrane systems. *Ind. Eng. Chem. Res.* **2016**, 55, 1995–2007.
- (47) Rall, D.; Schweidtmann, A. M.; Kruse, M.; Evdochenko, E.; Mitsos, A.; Wessling, M. Multi-scale membrane process optimization with high-fidelity ion transport models through machine learning. *J. Membr. Sci.* **2020**, *608*, 118208.
- (48) Ohs, B.; Lohaus, J.; Wessling, M. Optimization of membrane based nitrogen removal from natural gas. *J. Membr. Sci.* **2016**, 498, 291–301.
- (49) Zarca, R.; Ortiz, A.; Gorri, D.; Biegler, L. T.; Ortiz, I. Optimization of multistage olefin/paraffin membrane separation processes through rigorous modeling. *AIChE J.* **2019**, *65*, No. e16588.
- (50) Scholz, M.; Alders, M.; Lohaus, T.; Wessling, M. Structural optimization of membrane-based biogas upgrading processes. *J. Membr. Sci.* **2015**, 474, 1–10.
- (51) Chavez Velasco, J. A.; Tumbalam Gooty, R.; Tawarmalani, M.; Agrawal, R. Optimal design of membrane cascades for gaseous and liquid mixtures via MINLP. *J. Membr. Sci.* **2021**, *636*, 119514.
- (52) Taifan, G. S.; Maravelias, C. T. Generalized optimization-based synthesis of membrane systems for multicomponent gas mixture separation. *Chem. Eng. Şci.* **2022**, 252, 117482.
- (53) Ramírez-Santos, Á. A.; Bozorg, M.; Addis, B.; Piccialli, V.; Castel, C.; Favre, E. Optimization of multistage membrane gas separation processes. Example of application to CO<sub>2</sub> capture from blast furnace gas. J. Membr. Sci. **2018**, 566, 346–366.
- (54) Lee, S.; Binns, M.; Kim, J.-K. Automated process design and optimization of membrane-based CO2 capture for a coal-based power plant. *J. Membr. Sci.* **2018**, *563*, 820–834.
- (55) Arias, A. M.; Mussati, M. C.; Mores, P. L.; Scenna, N. J.; Caballero, J. A.; Mussati, S. F. Optimization of multi-stage membrane systems for CO<sub>2</sub> capture from flue gas. *International Journal of Greenhouse Gas Control* **2016**, 53, 371–390.
- (56) Chiwaye, N.; Majozi, T.; Daramola, M. O. On optimization of  $N_2$  and  $CO_2$ -selective hybrid membrane process systems for post-combustion  $CO_2$  capture from coal-fired power plants. *J. Membr. Sci.* **2021**, 638, 119691.
- (57) Engineering, and Medicine, A Research Agenda for Transforming Separation Science; The National Academies Press: Washington, DC, 2019; DOI: 10.17226/25421.
- (58) Hoffman, J. R.; Phillip, W. A. 100th anniversary of macromolecular science viewpoint: integrated membrane systems. *ACS Macro Lett.* **2020**, *9*, 1267–1279.
- (59) Werber, J. R.; Deshmukh, A.; Elimelech, M. The critical need for increased selectivity, not increased water permeability, for desalination

- membranes. Environmental Science & Technology Letters 2016, 3, 112–120.
- (60) Miettinen, K. Nonlinear Multiobjective Optimization; Springer Science & Business Media: New York, 2012; Vol. 12.
- (61) Dowling, A. W.; Ruiz-Mercado, G.; Zavala, V. M. A framework for multi-stakeholder decision-making and conflict resolution. *Comput. Chem. Eng.* **2016**, *90*, 136–150.
- (62) Zhang, P.; Yokoyama, T.; Itabashi, O.; Suzuki, T. M.; Inoue, K. Hydrometallurgical process for recovery of metal values from spent lithium-ion secondary batteries. *Hydrometallurgy* **1998**, *47*, 259–271.
- (63) Bynum, M. L.; Hackebeil, G. A.; Hart, W. E.; Laird, C. D.; Nicholson, B. L.; Siirola, J. D.; Watson, J.-P.; Woodruff, D. L. *Pyomo—Optimization Modeling in Python*, 3rd ed.; Springer International Publishing: Cham, Switzerland, 2021; Vol. 67.
- (64) Wächter, A.; Biegler, L. T. On the implementation of an interior-point filter line-search algorithm for large-scale nonlinear programming. *Mathematical Programming* **2006**, *106*, 25–57.
- (65) HSL, A collection of Fortran codes for large scale scientific computation. http://www.hsl.rl.ac.uk/, Date of Access: July 1, 2021.
- (66) Eugene, E. A.; Phillip, W. A.; Dowling, A. W. In Proceedings of the 9th International Conference on Foundations of Computer-Aided Process Design; Muñoz, S. G., Laird, C. D., Realff, M. J., Eds.; Comput.-Aided Chem. Eng.; Elsevier, 2019; Vol. 47; pp 469—474, DOI: 10.1016/B978-0-12-818597-1.50075-8.
- (67) Jabra, M. G.; Yehl, C. J.; Zydney, A. L. Multistage continuous countercurrent diafiltration for formulation of monoclonal antibodies. *Biotechnol. Prog.* **2019**, 35, No. e2810.
- (68) Siew, W. E.; Livingston, A. G.; Ates, C.; Merschaert, A. Continuous solute fractionation with membrane cascades—a high productivity alternative to diafiltration. *Sep. Purif. Technol.* **2013**, *102*, 1–14.
- (69) Muetzel, Z. W.; Ouimet, J. A.; Phillip, W. A. Device for the Acquisition of Dynamic Data Enables the Rapid Characterization of Polymer Membranes. *ACS Applied Polymer Materials* **2022**, *4*, 3438–3447.
- (70) Yaroshchuk, A.; Bruening, M. L.; Zholkovskiy, E. Modelling nanofiltration of electrolyte solutions. *Adv. Colloid Interface Sci.* **2019**, 268, 39–63.
- (71) Opong, W. S.; Zydney, A. L. Diffusive and convective protein transport through asymmetric membranes. *AIChE J.* **1991**, 37, 1497–1510.
- (72) Baker, R. W. Membrane Technology and Applications; John Wiley & Sons: West Sussex, England, 2012.
- (73) Mehta, A.; Zydney, A. L. Permeability and selectivity analysis for ultrafiltration membranes. *J. Membr. Sci.* **2005**, *249*, 245–249.
- (74) Huang, S.; Wu, M.-B.; Zhu, C.-Y.; Ma, M.-Q.; Yang, J.; Wu, J.; Xu, Z.-K. Polyamide Nanofiltration Membranes Incorporated with Cellulose Nanocrystals for Enhanced Water Flux and Chlorine Resistance. ACS Sustainable Chem. Eng. 2019, 7, 12315—12322.
- (75) Gao, F.; Hunter, A.; Qu, S.; Hoffman, J. R.; Gao, P.; Phillip, W. A. Interfacial junctions control electrolyte transport through charge-patterned membranes. *ACS Nano* **2019**, *13*, 7655–7664.
- (76) Somrani, A.; Hamzaoui, A.; Pontie, M. Study on lithium separation from salt lake brines by nanofiltration (NF) and low pressure reverse osmosis (LPRO). *Desalination* **2013**, *317*, 184–192.
- (77) Yang, Z.; Fang, W.; Wang, Z.; Zhang, R.; Zhu, Y.; Jin, J. Dual-skin layer nanofiltration membranes for highly selective Li+/Mg2+ separation. *J. Membr. Sci.* **2021**, *620*, 118862.
- (78) *IUPAC-NIST Solubility Database*, Version 1.1 NIST Standard Reference Database 106, 2012, DOI: 10.18434/T4QC79.
- (79) Armstrong, J. A.; Bernal, E. E. L.; Yaroshchuk, A.; Bruening, M. L. Separation of ions using polyelectrolyte-modified nanoporous tracketched membranes. *Langmuir* **2013**, *29*, 10287.
- (80) Qu, S.; Dilenschneider, T.; Phillip, W. A. Preparation of Chemically-Tailored Copolymer Membranes with Tunable Ion Transport Properties. ACS Appl. Mater. Interfaces 2015, 7, 19746.
- (81) Pagnanelli, F.; Moscardini, E.; Altimari, P.; Abo Atia, T.; Toro, L. Cobalt products from real waste fractions of end of life lithium ion batteries. *Waste Management* **2016**, *51*, 214–221.

- (82) Linneen, N.; Bhave, R.; Woerner, D. Purification of industrial grade lithium chloride for the recovery of high purity battery grade lithium carbonate. *Sep. Purif. Technol.* **2019**, 214, 168–173.
- (83) Agrawal, R. Membrane cascade schemes for multicomponent gas separation. *Industrial & Engineering Chemistry Research* **1996**, 35, 3607–3617.
- (84) Siew, W. E.; Livingston, A. G.; Ates, C.; Merschaert, A. Molecular separation with an organic solvent nanofiltration cascade augmenting membrane selectivity with process engineering. *Chem. Eng. Sci.* **2013**, 90, 299—310.
- (85) Wang, L.; Rehman, D.; Sun, P.-F.; Deshmukh, A.; Zhang, L.; Han, Q.; Yang, Z.; Wang, Z.; Park, H.-D.; Lienhard, J. H.; Tang, C. Y. Novel Positively Charged Metal-Coordinated Nanofiltration Membrane for Lithium Recovery. ACS Appl. Mater. Interfaces 2021, 13, 16906–16915.
- (86) Nan, J.; Han, D.; Zuo, X. Recovery of metal values from spent lithium-ion batteries with chemical deposition and solvent extraction. *J. Power Sources* **2005**, *152*, 278–284.
- (87) White, N.; Misovich, M.; Alemayehu, E.; Yaroshchuk, A.; Bruening, M. L. Highly selective separations of multivalent and monovalent cations in electrodialysis through Nafion membranes coated with polyelectrolyte multilayers. *Polymer* **2016**, *103*, 478–485.

### Recommended by ACS

## A Lithium Feedstock Pathway: Coupled Electrochemical Extraction and Direct Battery Materials Manufacturing

Jiangtao Hu, Dongping Lu, et al.

JUNE 30, 2022

ACS ENERGY LETTERS

READ 🗹

## Sustainable Production of Lithium Acetate by Bipolar Membrane Electrodialysis Metathesis

Chong-Yuan Zhong, Wei-Ming Zhang, et al.

APRIL 22, 2022

ACS SUSTAINABLE CHEMISTRY & ENGINEERING

READ 🗹

## Hydrophilic Modification Using Polydopamine on Core–Shell $\text{Li}_{1.6}\text{Mn}_{1.6}\text{O}_4@\text{Carbon}$ Electrodes for Lithium Extraction from Lake Brine

Yunhao Wang, Xu Xiang, et al.

JUNE 27, 2022

ACS SUSTAINABLE CHEMISTRY & ENGINEERING

READ [7]

### Mechanochemical Lithium Extraction and Zeolite Synthesis from End-of-Life Glass-Ceramics

Tobias Necke, Anke Weidenkaff, et al.

AUGUST 11, 2022

ACS SUSTAINABLE CHEMISTRY & ENGINEERING

READ 🗹

Get More Suggestions >